PERGAMON

International Journal of Multiphase Flow 25 (1999) 639–682

International Journal of Multiphase Flow

Two-point description of two-fluid turbulent mixing—II. Numerical solutions and comparisons with experiments

M.J. Steinkamp [1], T.T. Clark *, F.H. Harlow

Fluid Dynamics Group, T-3, Theoretical Division, Los Alamos National Laboratory, Mail Stop/B216, Los Alamos, NM 87545, USA

Received 24 March 1998; received in revised form 20 October 1998

Abstract

The spectral turbulence transport model from part I of these two articles is compared with experiments of the late stages of turbulent mixing due to Rayleigh–Taylor instability, when the dynamics become approximately self-similar in response to a constant body force. We also examine the spectral dynamics of the flow immediately following a rapid transient in the body force. Generic forms for anisotropic spectral structure are described and then used as a basis for deriving spectrally integrated moment equations that can be more easily incorporated into computer codes for scientific and engineering analyses. We describe comparisons with experiments of this spectral formulation and indicate directions for refinement, analogous to those that are required for constant density turbulence transport.

Keywords: Spectral turbulence transport model; Inhomogeneous turbulence; Variable density turbulence; Turbulent mixing; Interfacial instability; Two-phase turbulence; Rayleigh–Taylor instability; Two-phase flow

1. Introduction

The Rayleigh–Taylor instability occurs at the interface of two fluids of different densities configured such that the lighter fluid is accelerated into the heavier fluid by a pressure gradient, i.e. whenever the pressure gradient opposes the density gradient ($\nabla\bar{p}\cdot\nabla\bar{\rho} < 0$). This instability can occur, for example, in ICF targets during the laser implosion of a dense shell (pusher) filled with deuterium–tritium gas. The effects of this instability during the acceleration phase

* Corresponding author. Tel.: +1-505-665-4858; e-mail: ttc@lanl.gov.
[1] Present address: Engine Research, Technical Center F, Caterpillar Inc., Peoria, IL 61656-1875, USA.

0301-9322/99/$ - see front matter
PII: S0301-9322(98)00065-2

are of current interest to the ICF community (Takabe et al., 1985). For this study, we consider the incompressible case of the Rayleigh–Taylor instability where a body force due to an acceleration produces a pressure gradient across the fluid–fluid interface such that the higher pressure occurs in the lighter fluid. A quantitative overview of the Rayleigh–Taylor instability which describes the phenomenology that occurs at an unstable interface is given by Sharp (1984). The seminal work on this topic was that of Lord Rayleigh (1900), who was the first to investigate the equilibrium of a stratified inviscid fluid. Lamb (1931) discusses some problems related to Rayleigh's paper. Taylor (1950) generalizes the linear analysis and took into account inertial and body forces to include the effects of surface tension. Lewis (1950) experimentally confirms Taylor's findings by accelerating an initially stably stratified fluid downward at a rate 50 times greater than the acceleration due to gravity. This study by Lewis showed that, for an air–liquid interface, the linear analysis was correct for the initial stages of the instability. The experiment also shed some light on the large amplitude evolution of the instability.

This instability has been investigated using infinitesimal perturbations on the initial interface (Rayleigh, 1900; Lamb, 1931; Taylor, 1950; Allred and Blount, 1953; Birkhoff, 1954, 1956), as well as finite amplitude initial perturbations (Birkhoff, 1954, 1956; Emmons et al., 1960). The investigations have been extended to include the effects of surface tension (Bellman and Pennington, 1954), viscosity (Chandrasekhar, 1954; Hide, 1955), gradual density gradients (LeLevier et al., 1955; Case, 1960), as well as diffusion (Duff et al., 1962). Mitchner and Landshoff (1964) extended the above work to include the effects of compressibility. Richtmyer (1960) and Meshkov (1969) have investigated the instability resulting from an impulsively accelerated interface due to the passage of a shock. Richtmyer investigated the instability via small amplitude theory for a shocked interface, and Meshkov performed the validating shock tube instability experiments. Theoretical investigations of the late stage turbulent mixing of the Richtmyer–Meshkov instability include the work of Andronov et al. (1976).

Experiments that have concentrated on the growth of a single wavelength perturbation due to the Rayleigh–Taylor instability include the work of Emmons et al. (1960), Cole and Tankin (1973), Ratafia (1973), and Popil and Curzon (1979). Ratafia (1973) experimentally demonstrates the existence of Kelvin–Helmholtz roll-up structures on the sides of the interpenetrating spikes of the heavier fluid.

The first successful numerical calculations of the early stages of the Rayleigh–Taylor instability were performed by Harlow and Welch (1965) using their Marker and Cell (MAC) method for free surface calculations. Welch et al. (1966) describe a multifluid extension to the MAC method which was later used by Daly (1967) to study the influence of density variations and viscosity on the rate of growth and shape of the Rayleigh–Taylor instability. Daly found agreement with the predictions of Chandrasekhar (1954) for the growth rates in the linear regime. Daly investigated the evolution of a single wavelength initial velocity disturbance for various density ratios and established the now well-known behavior of a single wave at large amplitudes. For small density differences, Daly demonstrated the manner in which the interface rolls up into two counter-rotating vortices. For large density differences, the classical picture is seen of the spikes of the heavier fluid penetrating the lighter, which in turn, bubbles up around the interpenetrating spikes. Daly (1969) extends his work of 1967 to include the influence of surface tension on both the linear and the nonlinear phase of the instability.

Youngs (1984) describes the "basic picture of the mixing process" due to the Rayleigh–Taylor instability in which he identifies three stages of evolution for the instability. The first stage that he identifies corresponds to the appearance of the most unstable perturbation of wavelength λ_m which grows exponentially. Stage two of the evolution commences when the height of the perturbation is approximately half the value of the wavelength and is characterized by a slowing of the growth rate of the perturbations that penetrates the denser fluid to a rate proportional to $\sqrt{g\lambda}$, where g is the imposed acceleration. Stage two is characterized by the classical Rayleigh–Taylor picture of interpenetrating spikes and bubbles. If the initial perturbations are small, then it is the nonlinear coupling between the small scale structures that creates larger wavelengths. Experiments of Lewis (1950) and Emmons et al. (1960) show that it is a competition between bubbles that leads to a bubble amalgamation process where the larger bubbles crowd out the smaller ones. The velocity derived in the theory by Davies and Taylor (1949), $v = 0.66\sqrt{gR}$, also shows that the bubbles of larger radius will dominate the flow. In this article, we refer to this process by which dominant wavelengths increase in magnitude as "bubble doubling". These interactions facilitate the loss of detailed memory of the initial conditions. Memory of the initial conditions is lost when the dominant wavelengths of the perturbations are about 10 times larger than λ_m. This point marks the beginning of the final stage of evolution. The effects of viscosity diminish as the scale structures continue to grow.

In the final stage, the flow is defined as completely turbulent, and it is this mixing zone between the two fluids that is hereafter referred to as the turbulent mixing zone (TMZ). Since memory of the initial conditions is lost at the beginning of this stage, the flow is said to be self-similar. Consequently, the only remaining identifiable length scale of the flow is the quantity gt^2, where g is acceleration and t is time. Thus, the width W, of the TMZ can only be expressed as a product of this quantity and some function of the density, namely,

$$W = F\left(\frac{\rho_1}{\rho_2}\right)gt^2$$

Read and Youngs (1983) and Read (1984) use a rocket-rig apparatus at the United Kingdom Atomic Weapons Research Establishment (AWRE) in Aldermaston to investigate the final stage behavior of the mixing induced by the Rayleigh–Taylor instability. Also, Kucherenko et al. (1991) use a similar apparatus at the Soviet All-Union Research Institute of Technical Physics, at Chelyabinsk-70.

Data from AWRE and Chelyabinsk-70 are used as a basis for comparison in this article. These experiments and the numerical studies of Youngs (1984) confirm that the instability becomes self-similar during the last stage of growth.

By definition, the mixing width, W, of the TMZ is the algebraic sum of h_1 and h_2 such that, $W = h_1 + h_2$. By definition, h_1 is the difference in height between the position of the original perturbed interface and the position in the TMZ where the volume fraction of the heavy fluid has decreased from 1.0 to something near 0.95, i.e. near the edge of the bubble envelope; whereas h_2 is defined as the height difference between the position of the original perturbed interface and the position in the TMZ where the volume fraction of the light fluid has decreased from 1.0 to something near 0.05 (Read and Youngs, 1983; Smeeton and Youngs, 1987; Youngs, 1992a). The exact volume fraction that is used to determine h_1 and h_2 differs

among experimenters. Note that Kucherenko et al. (1991) use L_{21} to define the British value of h_2 and L_{12} to define the British value of h_1, but for simplicity, the data of Kucherenko et al. is expressed in terms of h_1 and h_2 within this report.

Both numerical simulations (Youngs, 1984, 1991) and experimental results (Read and Youngs, 1983; Read, 1984; Smeeton and Youngs, 1987; Youngs, 1992a) indicate that the above empirical expression for W is more applicable to the depth of penetration of the lighter fluid (bubble envelope) into the heavier fluid, h_1, than for the total width, W, of the TMZ. Read and Youngs (1983) and Burrows et al. (1984) show that if the mixing between the two fluids evolves from small random perturbations on the interface, the penetration of the mixing region into the denser fluid, h_1, is given by

$$h_1 = \alpha \frac{\rho_2 - \rho_1}{\rho_1 + \rho_2} g t^2$$

where the self-similarity coefficient α is found to be insensitive to the density ratio and varied little from a value of about 0.06 among different experiments (Read and Youngs, 1983; Read, 1984; Andrews, 1992; Linden et al., 1992). One final definition that is used throughout this report is that of the variable X, the scaled acceleration used in the above experiments, which is given by

$$X = \frac{\rho_2 - \rho_1}{\rho_1 + \rho_2} g t^2$$

The best experimental estimates for α in a truly three-dimensional situation are approximately 0.07. Youngs (1992a) gives a range of values from 0.050 to 0.077 for α. Linden et al. (1992) report a value of 0.070 for α when using a relatively large, three-dimensional tank. Andrews and Spalding (1990) cite a value of 0.04 for α. Snider and Andrews (1994), who report values of $\alpha = 0.070 \pm 0.011$, explain that the container used to hold the mixing fluids of the experiment of Andrews and Spalding (1990) was narrow (approximately "two-dimensional"), and that this could account for the smaller value of α. On average, the values of α are higher for three-dimensional tests than those values of α found in "two-dimensional" tests. Youngs confirms this numerically; for two-dimensional numerical calculations, Youngs (1991, 1992a) reports values of α between 0.04 and 0.05, while the early time values of α are reported as higher for the three-dimensional case (Youngs, 1991). Others have numerically investigated the evolution of the TMZ (Gardner et al., 1988; Tryggvason and Unverdi, 1990; Andrews, 1992; Glimm et al., 1992; Li, 1993), and have all reported values of α close to the above values reported by Youngs, i.e. $0.038 \leq \alpha \leq 0.071$.

It should be mentioned that, in the literature, Kucherenko et al. use a self-similarity variable, S, defined as $S = gt^2/2$, but the data from Chelyabinsk-70 which we use in this article is for a density ratio, n, of 3, and coincides with an Atwood number, $(\rho_2 - \rho_1)/(\rho_1 + \rho_2)$, of 0.5. Thus, the self-similarity variable X from AWE and the S from Chelyabinsk-70 are identical for the results presented in this work.

Demixing has also been investigated (Smeeton and Youngs, 1987; Kucherenko et al., 1994). Kucherenko et al., as well as Smeeton and Youngs, accomplish this by changing the acceleration during the self-similar stage of growth of the TMZ. They observe a partial contraction in the width of the TMZ and define a constant to accompany this process which is

similar to the acceleration constant of α as described above. They cite values for this constant on the order of 1/7 of the values of α. Other variants of the change in acceleration are reported by Smeeton and Youngs (1987). Spalding (1985b) used a direct numerical simulation (DNS) to study this de-mixing process. Andrews (1986), as suggested by Spalding (1985a), used a two-fluid model to predict both the Rayleigh–Taylor mixing and the late time de-mixing.

Andrews (1986) states that the use of a two-fluid model is justified because the TMZ is comprised of fragments of different density fluids. A body force induces different accelerations on each fluid fragment causing different relative fluid velocities, and, hence, different interfluid drags. Andrews paraphrases Spalding (1985a) by referring to this phenomena as "sifting" and suggests the use of a two-fluid model to capture correctly the relative motion of the fluid fragments. A two-fluid model, as opposed to a turbulence model which uses diffusive-type gradient approximations for closure of the triple correlation terms, is necessary to capture the effects of a counter-gradient flux. Youngs (1992b) also uses a two-fluid model to investigate the turbulent mixing of the late stages of the Rayleigh–Taylor instability. He finds good agreement with his own experiments. For these same reasons, we also incorporate concepts pertaining to interfluid drag from a two-fluid model into our investigations as described in the first of these two articles, which will hereafter be referred to as Article I. For a comprehensive summary on two-phase flow modeling, the reader is referred to Drew (1983).

Many investigators have used single-point variable density turbulence transport models to investigate the late stages of the Rayleigh–Taylor instability (Belenkii and Fradkin, 1965; Anuchina et al., 1978; Neuvazhaev and Yakovlev, 1984; Andrews, 1986; Kucherenko and Shibarshov, 1986; Anisimov and Polyonov, 1989; Neuvazhaev, 1989; Polyonov, 1989; Nikiforov, 1991). Reasonable agreement with experiment is easily achievable with the adjustment of parameters, but their results are not universal due to the implicit assumptions of statistical equilibrium. Another problem with single-point models is the diffusive nature of the closure assumptions. These diffusive closures do not allow for the proper representation of de-mixing (Andrews, 1986) due to transients in the flow. To address this problem, investigators have tried to form hybrid models using both the single-point transport models combined with the equations of two-fluid models (Cranfill, 1991; Youngs, 1989, 1992b).

An avenue that has proved useful in simulating the early stages of the Rayleigh–Taylor instability is numerical simulation using front tracking (or interface tracking) methods (Tryggvason, 1988; Li, 1993; Linden et al., 1994; Youngs, 1994). Also, the presence of widely varying length scales makes high Reynolds number turbulence very expensive, if not impossible, to simulate using DNS. The investigator must have a sufficiently resolved grid in order to compute correctly the transfer of energy to the finest scales of the flow. Due to the complexity of the structures after the self-similar stage has been reached, these methods tend to become very expensive numerically, and one finds motivation to approach the problem from a statistical point of view.

To this date, however, only Besnard et al. (1995), Clark and Spitz (1995), and our work in Article I represent the development of a statistical spectral model for variable density turbulent mixing. Our spectral model is capable of describing a turbulent flow that is far from statistical equilibrium and allows for the examination of the statistical equilibrium, or "self-similar" phase of mixing. This capability goes beyond that which any single-point model may claim.

In this article, we present the numerical results of the spectral model equations from Article I as applied to turbulent mixing due to the Rayleigh–Taylor instability. The purpose of this article is to demonstrate the behavior of the spectral model equations, show comparisons with experiments, and show the effect of some variations to the base case calculation. For this demonstration, we will present numerical results of a base case for mixing only, followed by examples to demonstrate the influence that the various coefficients have on the calculations. We also show the spectral behavior for the net mass flux velocity, **a**, during the process of a rapid transient (an acceleration reversal is used for this demonstration). The latter example demonstrates the spectral behavior for flows that are no longer in spectral equilibrium.

To study the properties of the spectral equations we have written a finite-difference code for their numerical solution. The configuration we have chosen for illustration (Rayleigh–Taylor instability) is that of an initial interface between two inviscid, incompressible fluids of different densities. The fluid is subjected to a body force, $\rho\mathbf{g}$, due to an acceleration directed in the negative y direction. The pressure gradient arises by imposing a body force (acceleration) to the fluids but holding the containing vessel at rest. An equivalent procedure, employed by the experiments with which we compare, accelerates the vessel, with a pressure gradient arising in order that the fluid is accelerated commensurate with the motion of the vessel. Below the mixing layer is a fluid with density ρ_1; above the layer is a different fluid with density ρ_2; for all of our calculations $\rho_1 < \rho_2$, such that when $\mathbf{g} < 0$ the configuration is unstable and mixing ensues. We also discuss the consequences of a reversal of the sign of **g** after the mixing layer has become self-similar.

The numerical solution technique and its validation for the present purpose is described by Steinkamp (1996). The computer code consists of a spectral part and a spectrally integrated part. In the latter, with the containing vessel at rest, the pressure gradient is updated in such a manner as to ensure vanishing flux of fluid volume in all cells within the flow. Thus the transport equations for $\tilde{\mathbf{u}}$ and the spectrally integrated transport equation for **a** are forced to be equivalent, which determines the variations of pressure in response to the specified body force. Due to the chosen configuration and imposed acceleration, the mean flow variables exhibit only y-dependence and the only nonzero components of the turbulence variables are R_{nn}, R_{yy}, a_y, and of course b, since it is a scalar measure of the degree of mixing within each computational cell. Hereafter, we will use R_{ij}, a_y and b to indicate the spectral quantities and we will explicitly show their respective arguments only for the case of representing their single-point forms, i.e. when they are functions of the normal direction y and time only. Whereas the density, ρ, velocity, **u**, pressure, p, turbulent length scale, S, and the turbulent kinetic energy, K, will always be functions of the normal direction y and time only, the acceleration, **g**, varies only with time for these discussions.

The principal data for comparison with calculations comes from extensive experimentation at AWRE (Smeeton and Youngs, 1987) and Chelyabinsk-70 (Kucherenko et al., 1991). The data are not as complete as we would like; we expect considerably more data from the anticipated experiments of Remington and Dimonte at Lawrence Livermore National Laboratory, LLNL (personal communication 1995). The results currently available are profiles of estimated mix fraction across the layer, the mix interpenetration rates into each fluid, and some qualitative indications of dominant scale.

2. Mixing due to an acceleration

Figures 1–12 give results from the base-case calculation. Dimensionality is denoted on each graph using L for a length scale, M for mass, and T for time. In the following figures, the spectral behaviors of the variables are plotted as functions of the nondimensional variable z, where $z = \ln(k/k_0)$. This logarithmic transformation is used to accentuate the regions of physical significance; that is to say, as the turbulence evolves, the turbulent length scales grow, corresponding to a migration of the turbulence spectra toward $k = 0$. Thus the transformation allows the details of the spectrum near $k = 0$ to be spread over the corresponding infinite interval in nondimensional z-space. The constant k_0 serves to nondimensionalize the transformed spectral equations and to provide a reference wave number for specifying initial conditions. The initial configuration consists of a heavy fluid ($\rho_2 = 2.0$) sitting over a lighter fluid ($\rho_1 = 1.0$). At time $t = 0$, acceleration ($g = -1.0$) is turned on, and the mixing of the two fluids commences. The nonlocal version of the source term is used in the Reynolds-stress equations (see Article I). At $t = 0$, the values of R_{nn}, R_{yy} and a_y are zero in every computational cell. The value of b likewise vanishes in every cell except the one containing the two-fluid interface, where

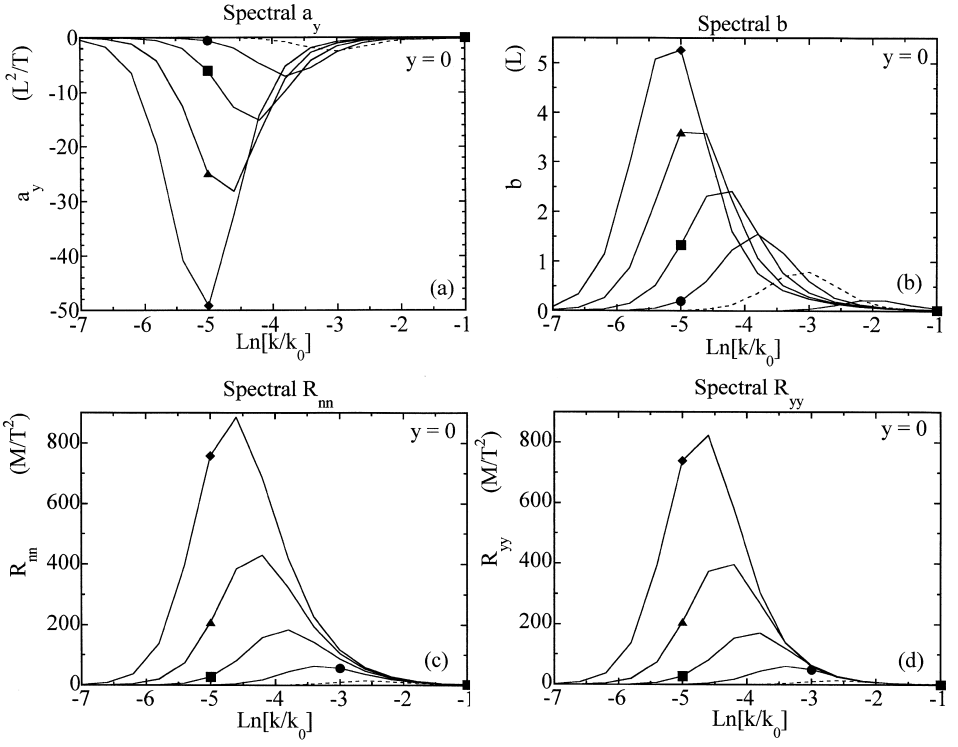

Fig. 1. Spectra at times, $t = 10$ (solid line, no symbols), 20 (dotted line, no symbols), 30 (circles), 40 (squares), 50 (triangles) and 60 (diamonds), at the position of the initial fluid interface for: (a) the net mass-flux velocity, a_y; (b) the specific volume–density correlation, b; (c) the contraction of the Reynolds stress tensor, R_{nn} and (d) the R_{yy} component of the Reynolds stress tensor.

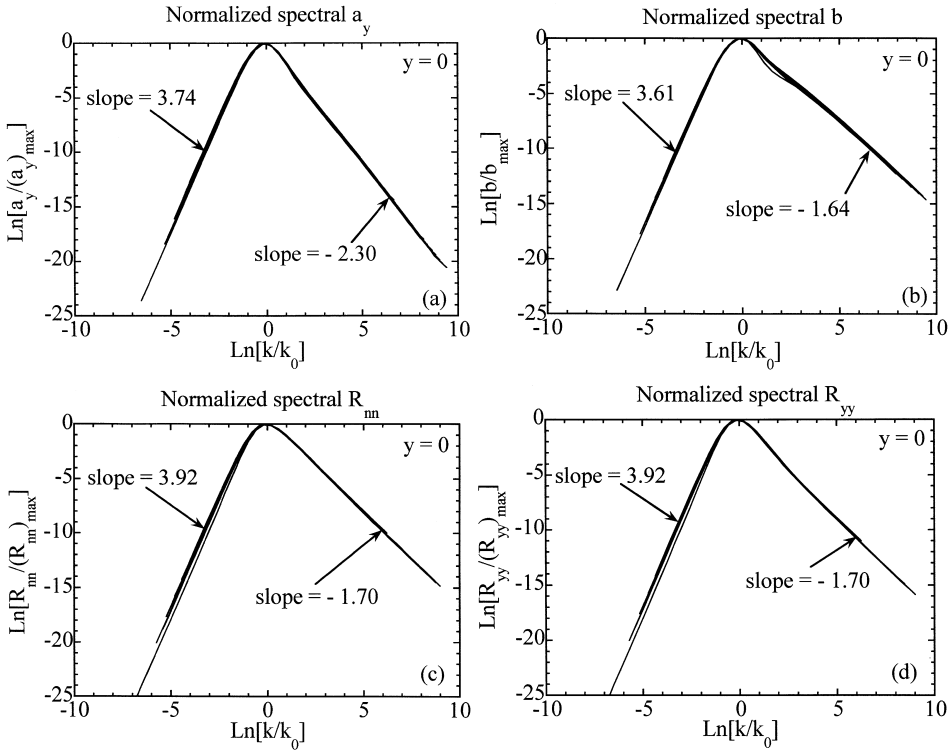

Fig. 2. Normalized spectra for $t = 30$, 35, 40, 45, 50, 55, 60 and 65, at the position of the initial fluid interface: (a) the net mass-flux velocity, a_y; (b) the specific volume–density correlation, b; (c) the contraction of the Reynolds stress tensor, R_{nn} and (d) the R_{yy} component of the Reynolds stress tensor.

$$b = \frac{\gamma_1 k^m}{1 + \gamma_2 k^{m+5/3}} \tag{1}$$

The two coefficients, γ_1 and γ_2, have been chosen to ensure that the maximum of b occurs at $k = k_0$ and the spectral integral of b, namely $b(y)$, has the maximum configurational value corresponding to equal volume fractions of the two fluids in that cell, i.e. $\theta_1 = \theta_2 = 0.5$,

$$b(y, t) = \frac{(\rho_2 - \rho_1)^2}{4\rho_1\rho_2} \tag{2}$$

For a discussion on the configurational value of $b(y,t)$, see Besnard et al. (1992). For the base case, $m = 4.0$, $k_0 = 1.0$, and

$$\gamma_1 = \frac{(\rho_1 - \rho_2)^2}{4\rho_1\rho_2 f(m)}$$

$$\gamma_2 = \left(\frac{3m}{5}\right) k_0^{-(m+5/3)} \tag{3}$$

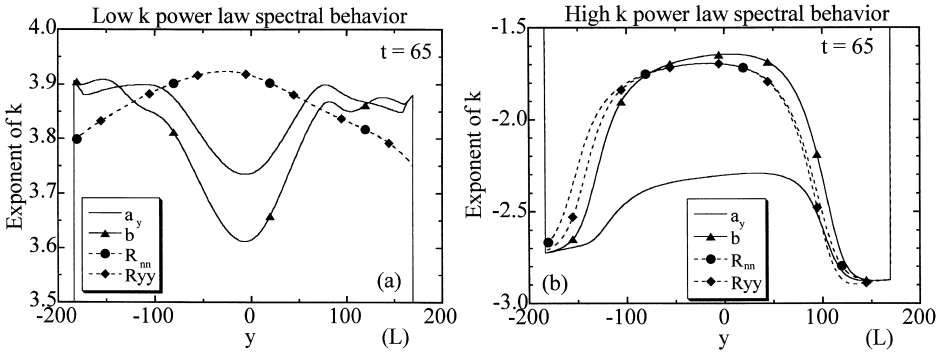

Fig. 3. Profiles of the power law exponent across the TMZ at $t = 65$ for (a) the low wave numbers; and (b) the high wave numbers.

where

$$f(m) = \int_{-\infty}^{+\infty} k^m \left(1 + \left(\frac{3m}{5}\right)\left(\frac{k}{k_0}\right)^{m+5/3}\right)^{-1} \mathrm{d}k \tag{4}$$

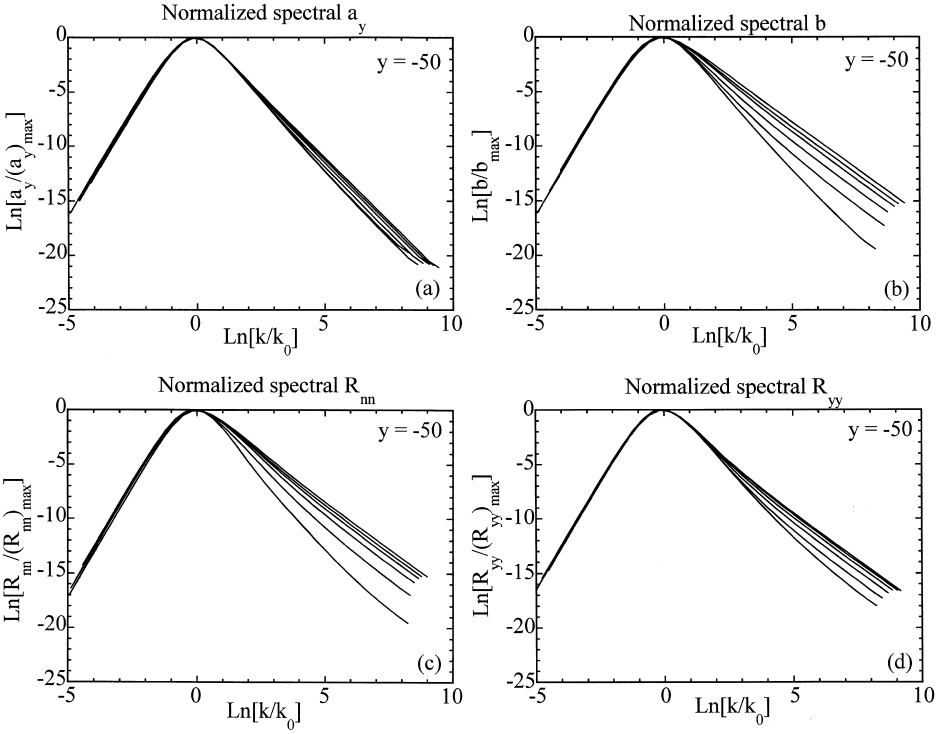

Fig. 4. Normalized spectra for $t = 30$, 35, 40, 45, 50, 55, 60 and 65, a distance of 50 units of length below the centerline of the TMZ: (a) the net mass-flux velocity, a_y; (b) the specific volume–density correlation, b; (c) the contraction of the Reynolds stress tensor, R_{nn} and (d) the R_{yy} component of the Reynolds stress tensor.

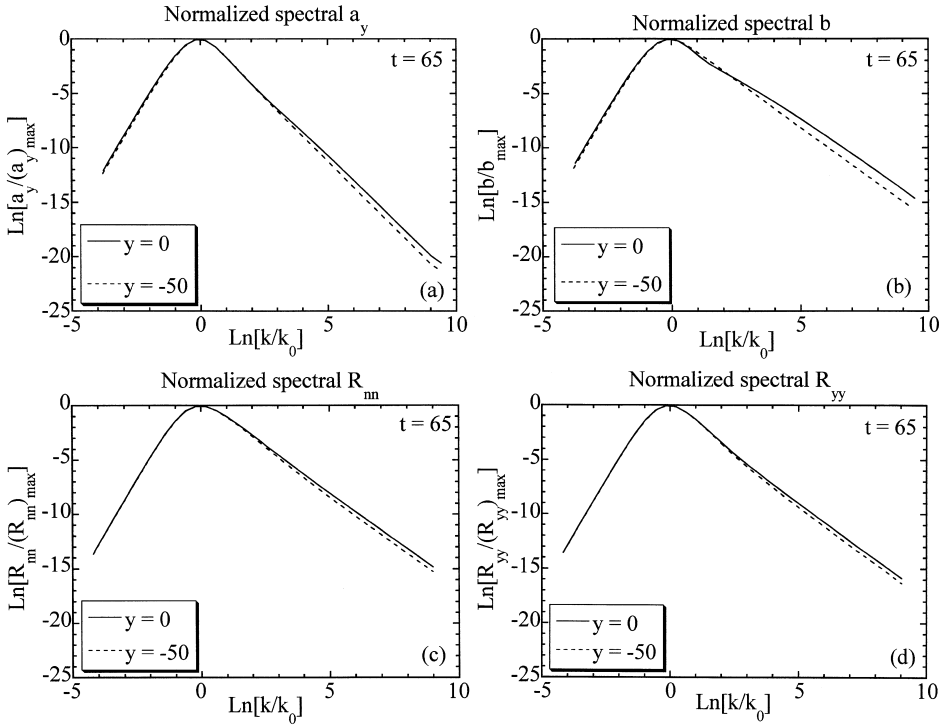

Fig. 5. Comparison of normalized spectra at $y = 0$ and $y = -50$ at $t = 65$ for: (a) the net mass-flux velocity, a_y; (b) the specific volume–density correlation, b; (c) the contraction of the Reynolds stress tensor, R_{nn} and (d) the R_{yy} component of the Reynolds stress tensor.

Boundary conditions must be considered whenever a calculation is performed. In the y direction the domain simply extends well into the pure material on either side of the TMZ, where everything is assumed to be at rest. In k-space we assume that the resolved part of the calculation is bounded by exponential behaviors for both the large and small wave numbers beyond the resolved region. This prescription allows the variable to flux through the k-space boundaries. We also experiment with an exception to this procedure, in which the flux of b at large wave numbers was set equal to zero, corresponding to (presumably) immiscible fluids with surface tension effects. As illustrated and discussed below, the effect on b is large; but the difference is almost entirely due to the retention or discarding of the high wave number, essentially passive parts of the b spectrum; and the effects on all the other quantities are negligible.

Values for the C coefficients in the transport equations of Article I have been chosen to be the same as those used by previous investigators for constant-density or single-point studies. For the drag coefficients in the a_y-equation, we use values that are greatly enhanced (Youngs, 1992b) over those for isolated spheres, as discussed in Article I. Hence, the values we use for the two drag coefficients are $C_{\mathrm{rp1}} = 5.0$ and $C_{\mathrm{rp2}} = 6.0$. For the local cascade coefficients, we use the values discussed by Clark and Zemach (1995): $C_1 = 0.1212$ and $C_2 = 0.0606$. Spatial diffusion and molecular diffusion are modulated by the coefficients, $C_{\mathrm{d}} = 0.03$ and $C_{\mathrm{db}} = 0.0$,

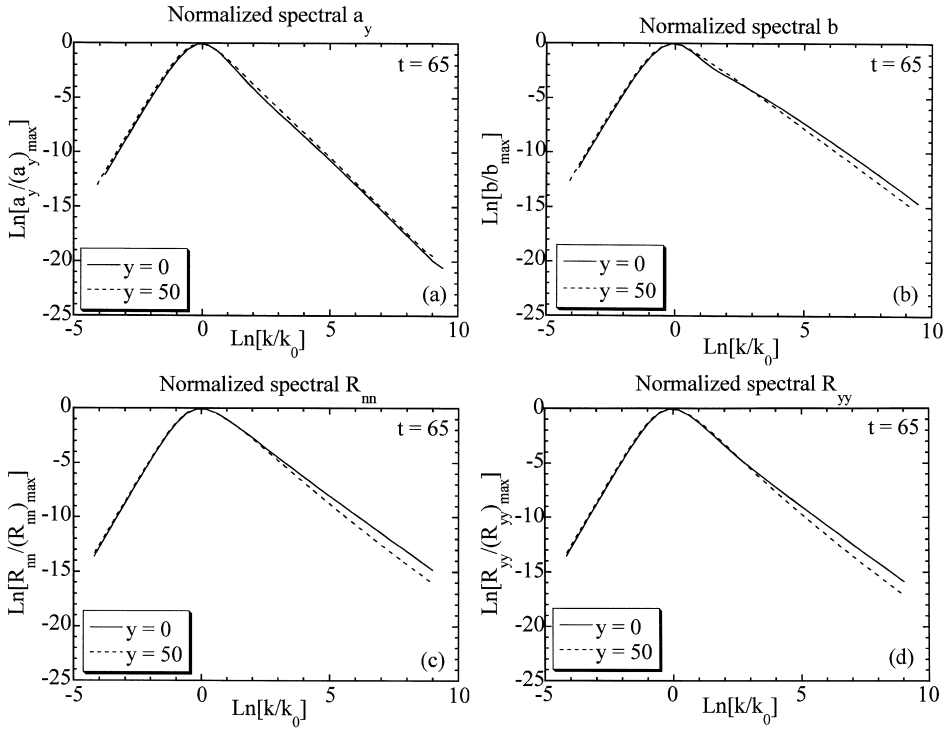

Fig. 6. Comparison of normalized spectra at $y = 0$ and $y = 50$ at $t = 65$ for: (a) the net mass-flux velocity, a_y; (b) the specific volume–density correlation, b; (c) the contraction of the Reynolds stress tensor, R_{nn} and (d) the R_{yy} component of the Reynolds stress tensor.

respectively. To match experiment, we found $C_{\mathrm{fb}} = 0.5$ to give decent agreement. Because C_{fb} is the one coefficient that is not ascertained in terms of previous investigations, we varied its value to determine the effect and observed that it is noticeable but not profound, as described below. Clark and Zemach (1995) discuss a value of C_{m} for constant density turbulence that is smaller than the value used here. We have tested the model for values of C_{m} between that suggested by Clark and Zemach (1995), $C_{\mathrm{m}} = 0.17$, and the value we use here, $C_{\mathrm{m}} = 1.0$, and found negligible differences in the results. We suspect that this is caused by the fact that our inhomogeneous flow is strongly dominated by the sources due to mixing that renders the return to isotropy a second-order effect.

Fig. 1 illustrates the time evolution of the spectral behavior for the variables as functions of the logarithm of (k/k_0). In all four plots the spectra are migrating to the left (toward lower k values) as time progresses. We identify length scales as the reciprocal of the wave number at which the spectrum has its extremum. The leftward migration is thus consistent with an increasing length scale for each variable. The spectra are given for equal time increments, $\Delta t = 10$, so as to demonstrate the linearly increasing growth rate of the peaks of the spectra. This variation is consistent with quadratic growth in time of the TMZ width, in agreement with expected self-similar behavior as described in the Appendices.

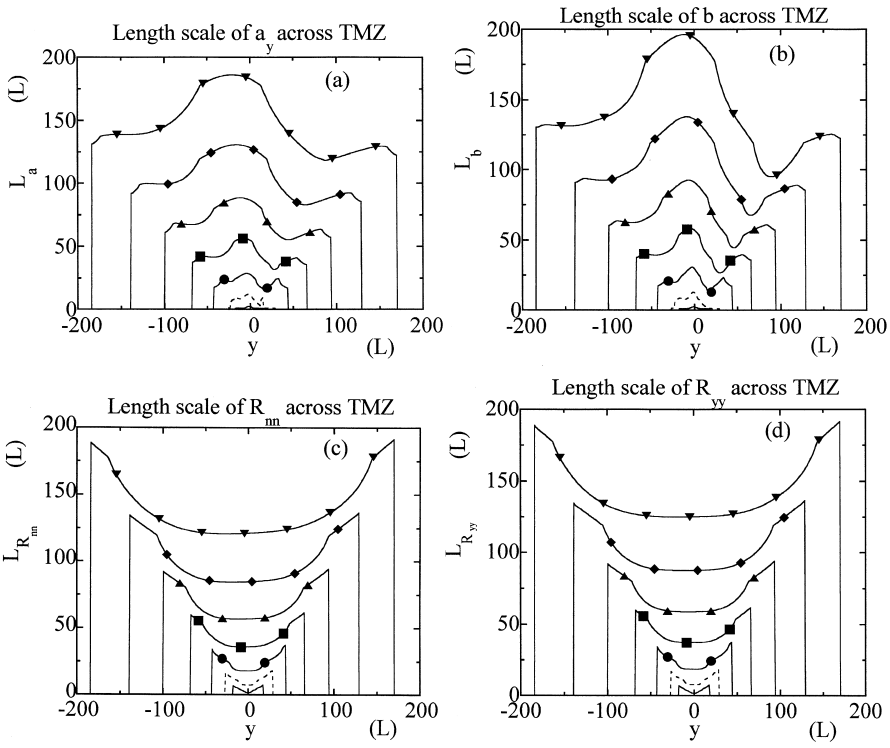

Fig. 7. Profiles of the length scales across the TMZ at $t = 5$ (solid line, no symbols), 15 (dotted line, no symbols), 25 (circles), 35 (squares), 45 (triangles), 55 (diamonds) and 65 (upside-down triangles) for: (a) the net mass-flux velocity, a_y; (b) the specific volume–density correlation, b; (c) the contraction of the Reynolds stress tensor, R_{nn} and (d) the R_{yy} component of the Reynolds stress tensor.

One characteristic that demonstrates the intervariable relationships that exist within the equations is the differing behavior of the spectral structures at the higher wave numbers. The right sides of the spectra for a_y and b migrate rapidly toward smaller values of k causing an overlapping appearance for a sequence of plots, while the right sides of the spectra for R_{nn} and R_{yy} coincide for that same sequence of times. The strong migration to the left seen in the b spectrum is due to the relatively large value chosen for C_{fb}, the one "free" parameter in our equations. The value of C_{fb} significantly influences the leftward migration of the spectrum of b. This effect influences the b spectrum the most. Because b is a principal source to a_y, the effect is also seen in the spectrum of a_y but to a relatively lesser degree. The Reynolds-stress spectra are, in turn, also moved to lower wave numbers. This leftward migration of these spectra is associated with the nonlinear "bubble-doubling" in the mixing layer, as observed in numerous experiments and DNS calculations, and is important for the agreement with experiments described below. These overall spectral forms result from a complicated interplay among physical processes represented by the terms in the equations. In Article I we show in much more detail the origins for the behaviors described in this base-case calculation and its variants.

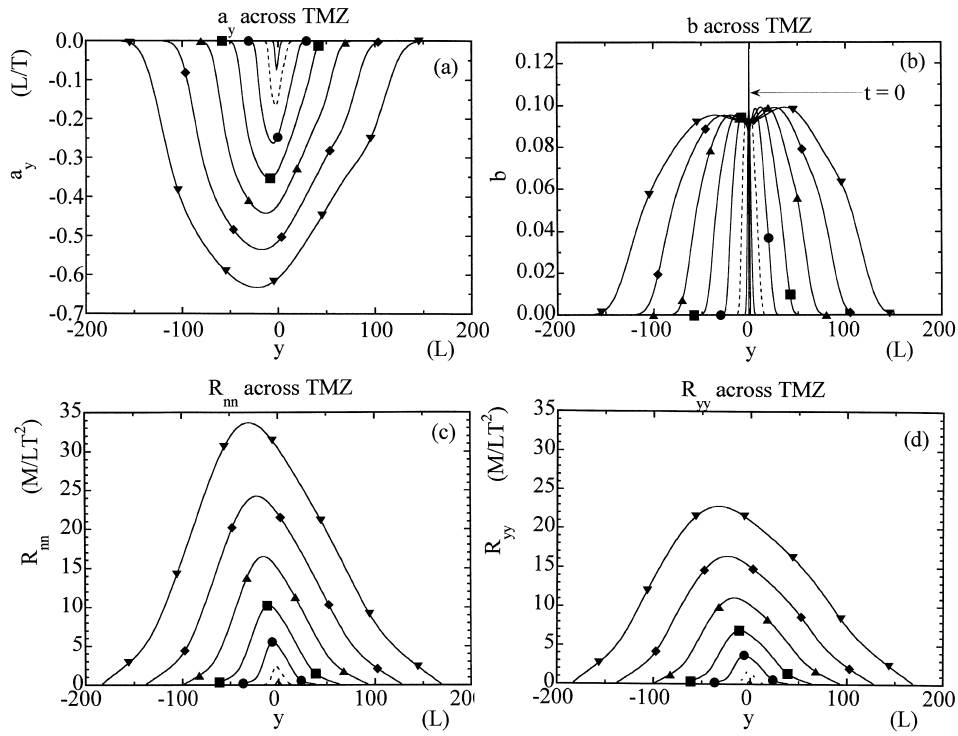

Fig. 8. Profiles of spectrally integrated variables across the TMZ at $t = 5$ (solid line, no symbols), 15 (dotted line, no symbols), 25 (circles), 35 (squares), 45 (triangles), 55 (diamonds) and 65 (upside-down triangles) for: (a) the net mass-flux velocity, a_y; (b) the specific volume–density correlation, b; (c) the contraction of the Reynolds stress tensor, R_{nn} and (d) the R_{yy} component of the Reynolds stress tensor. The values for $t = 65$ are designated by the dotted line.

The self-similar nature of the spectral evolution of Fig. 1 can be demonstrated by rescaling the results as shown in Fig. 2. The results in Fig. 2 are normalized to enable us to compare the shapes of these plots at successive times. The resulting normalized plots are called "shape plots". To achieve this normalization, two steps are taken. First, a spectrum is divided by its extremum, resulting in all of the spectral maxima coinciding with 1.0 and values of the entire spectrum falling between 0 and 1. Next, the spectra are all shifted so that the maximum of the spectra coincide with $k = k_0$. A sequence of times of these resulting shape plots is given on the same graph so as to identify any differences in their structures. The coincidence of all plots indicates a self-similar evolution of the mixing layer. The plots of Fig. 2 are taken from the cell where the initial fluid interface existed. The mixing evolution becomes self-similar near $t = 30$, as demonstrated by the overlapping plots of this figure.

As the spectral peak migrates to the left, less and less of the spectrum lies to the left of that peak and more of the resolved spectrum lies to the right. When the spectra are then shifted in the normalizing process, the appearance of a diminishing tail on the left side and an increasing tail on the right side is observed. Thus the plot with the longest tail on the left side represents the earliest time of the sequence and the plot with the longest tail on the right side represents

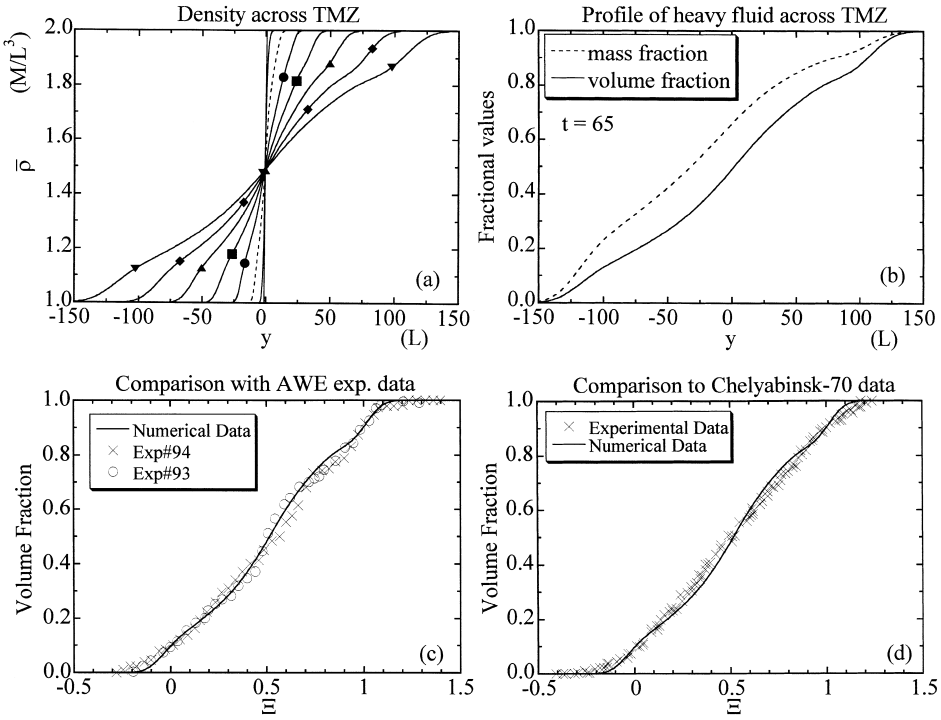

Fig. 9. (a) Profiles of density across the TMZ for $t = 0$ (solid line, no symbols), 5 (solid line, no symbols), 15 (dotted line, no symbols), 25 (circles), 35 (squares), 45 (triangles), 55 (diamonds) and 65 (upside-down triangles). (b) Mass and volume fractions of the heavy fluid across the TMZ at $t = 65$. (c) Comparison of numerical results with AWE experimental data (Smeeton and Youngs, 1987 (Fig. 24 and 25)). (d) Comparison of numerical results with Chelyabinsk-70 experimental data (Kucherenko et al., 1991 (Fig. 11)).

the latest time in the sequence. The slopes at low and high wave numbers are given to demonstrate the behaviors of the spectral variables. It is especially noteworthy to observe here the very close achievement of self-similarity.

The slopes in Fig. 2 represent the power law behavior of the spectra at only the initial position of the fluid interface, $y = 0$. Since these plots are functions of the logarithm of (k/k_0), the slope of the line corresponds to the power, m, of the wave number, k. (These are slopes near $k = 0$ and represent modifying tendencies for low wave numbers near $k = 0$, but not at precisely $k = 0$, where the initial value of m is preserved). The spatial variation of the value of m across the TMZ for both the low and high wave numbers is shown in Fig. 3. This plot is given for $t = 65$ well after the establishment of self-similarity. In effect, the spatial variations shown in Fig. 3 indicate the temporal evolution of the power laws for any one fixed position. The center of the plot ($y = 0$) has been developing the longest, and the edges of the TMZ are, relatively speaking, the newest parts.

For the low wave numbers, the b spectrum has a smaller value of m near $y = 0$ than occurs for the other spectra. The explanation lies in the effects of the C_{fb} term, which gives to b the leading role in describing the nonlinear "bubble-double" process. Initialized with k^4

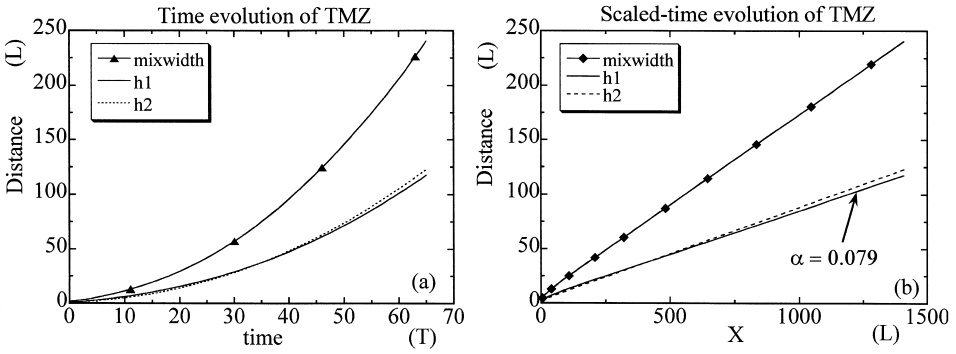

Fig. 10. Spikes, h_2, and the bubbles, h_1, (a) as functions of time, and (b) as functions of the similarity variable, X.

variation near $k = 0$, the b spectrum feels most strongly the modifying effects of leftward (in k-space) propagation of a concave-downwards structure that decreases the exponent. With b as a source to a_y, and a_y as a source to R_{ij}, the decrement in exponent is successively less in these latter two functions. This behavior and the behaviors of both the a_y and the R_{ij} spectra are consistent with the overlapping seen in Fig. 1. The high wave number, power-law behavior of the four variables coincides at the edges of the TMZ and then separates as time evolves. The values of m for the high wave numbers of Fig. 3(b) at $y = 0$ are equal to the slopes of the plots in Fig. 2. Only near $y = 0$ does one observe the classical values of $m = -5/3$ (for b and R_{ij}) and $m = -7/3$ for a_y, which result from the constancy of cascade flux for b, R_{nn} and R_{yy} and the balance of drag with production for a_y, as discussed in more detail in Article I.

Fig. 4 shows the evolving spectral forms at a distance of 50 units of length below the initial interface, showing the manner of arrival of the spectrum at each station as the TMZ widens. The spectrum of a_y arrives at nearly its self-similar form for all wave numbers, whereas the spectra for the other quantities arrive in self-similar forms only for the lower wave numbers; at

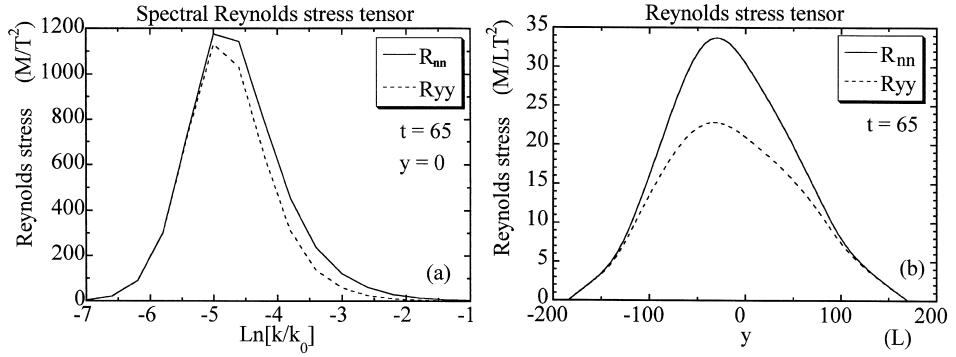

Fig. 11. Comparison of the trace of the Reynolds stress tensor, R_{nn}, with R_{yy} for: (a) the centerline, $y = 0$, at $t = 65$, and (b) the spectrally integrated form across the TMZ.

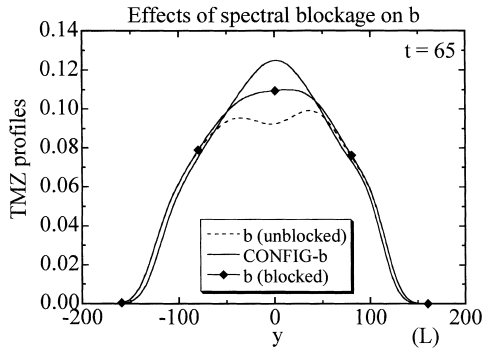

Fig. 12. Profile of b across the TMZ for the case of a spectrally unblocked calculation and a spectrally blocked calculation compared with the configurational calculation of b, at $t = 65$.

the higher wave numbers there is significant lag in the establishment of spectral self-similarity. There are two reasons for this behavior. One of these is the effect of nonlocal source for R_{nn} and R_{yy}, which projects the low wave number effects into lateral regions well ahead of the effects at high wave numbers.

The second reason is that the growth of spectral forms for b, R_{nn} and R_{yy} is at first dominated by the effects of sources which at any station tend initially to impart a $k^{-7/3}$ form at high wave numbers, being thereafter altered to $k^{-5/3}$ as the effects of constant cascade flux begin to dominate.

Fig. 5 shows a comparison at $t = 65$ of the spectral form functions at $y = 0$ and $y = -50$. By this time the self-similar form has been completely reached at $y = 0$ and nearly reached at 50 units of length below $y = 0$. Their nearly identical forms serve as a conformation of the self-similar hypothesis discussed in Appendix A. Fig. 6 illustrates a similar comparison at $y = 50$ units above the initial interface, again confirming the remarkable observation of the form-function decomposition hypothesis described in Appendix A.

This decomposition is possible because of neglect of molecular effects and surface tension. It should be emphasized that the spectral normalizations to unit magnitude and shift to $k = k_0$ have occurred over very large and different ranges in these figures, so that their coincidence seems all the more remarkable. We believe that there is a powerful underlying scaling principle that can be exploited in the systematic analysis of certain turbulence circumstances that are inhomogeneous, anisotropic, and even have large variations in fluid density.

Fig. 7 illustrates the nature of k shift that has been employed in getting the preceding plots of spectral form functions. In this figure we show the reciprocal of the wave number at which each spectrum has a maximum as a function of position across the TMZ. The ordinate is thus a length scale, which relates the length scale proportional to $K\sqrt{K}/\varepsilon$ that occurs in single-point K–ε turbulence transport models. Structural details in these length-scale profiles have their origin in the initialization for calculations where we only initialize the one cell containing the original fluid–fluid interface, which is far from self-similar. These minor details, once established during the early-time adjustments to self-similarity, are captured and maintained by the achievement of that self-similarity, indeed confirming the attainment of that state. Of more substance, however, are the overall forms of these plots. The length scales for a_y and b more-

or-less decrease towards the edges of the mixing layer, whereas the length scales for R_{nn} and R_{yy} increase.

The basic reason for the laterally increasing length scales for Reynolds stress can be traced to the nonlocal source. This identification is confirmed by contrasting with the results for a local source term; see Section 4, which contains figures that show a lateral decrease in scale for R_{nn} and R_{yy}. The significance of this effect for single-transport modeling is the lack of proportionality among length scales, for which we obtain remediation by allowing for more than one scale to arise in the moment derivations. (This generalization becomes even more significant in the non-self-similar response to rapid transients of drive.)

Self-similarity also occurs in physical space, as shown in Fig. 8, again confirming the hypothesis stated in Appendix A. The initialization of b at $y = 0$ is seen as the spike at $t = 0$. Lateral "wings" on the Reynolds-stress profiles arise as a consequence of the nonlocality of the creation term.

Fig. 9 describes the numerical results in terms of observables that can be compared with experimental data. The principal data are the depth of penetration of heavy fluid into light, h_2, of light fluid into heavy, h_1, and the variations of relative concentration between these edges of the TMZ. In this figure we describe the concentration profiles in terms of mean density, $\bar{\rho}$, together with the mass fraction and volume fraction of the heavier material. As pointed out by a Russian experimental group (Kucherenko et al., 1991), the most convenient way to illustrate the profile shape is to plot volume fraction as a function of the reduced variable

$$\Xi \equiv \frac{y - y_{0.1}}{y_{0.9} - y_{0.1}} \tag{5}$$

where $y_{0.1}$ and $y_{0.9}$ are the positions at which the volume fraction is 0.1 and 0.9, respectively. The excellence of agreement with both the British and Russian experimental data is not as trivial as the simple structure of the profiles would suggest. Two-field transport theory also achieves this degree of agreement (Steinkamp, 1996), but the single-point turbulence transport calculations using the model of Besnard et al. (1987) have great difficulty in matching this simple profile of volume fraction across the TMZ without resorting to an ad hoc modification of the transport equation for the mass flux.

The plots as functions of Ξ in Fig. 9 exhibit the structure but preclude the observation of behavior for $h_1(t)$ and $h_2(t)$. These quantities are shown in Fig. 10 as functions of time and of the similarity variable,

$$X = \frac{(\rho_2 - \rho_1)gt^2}{(\rho_1 + \rho_2)} \tag{6}$$

From an experimental viewpoint, the evolution of h_1 and h_2 depends on how the edges of the TMZ are located. The same comment applies to the calculation results. As shown by the Russian experimentalists (see Section 4), edge criteria at volume fractions of 0.01 and 0.99 (fine-edge criteria) result in much larger values of h_1 and h_2 (and of h_2/h_1) than criteria at volume fractions of 0.1 and 0.9 (coarse-edge criteria). They also show, and we confirm, that the ratio h_2/h_1 converges very slowly to asymptotic value, being highly dependent on the early-time rate of approach to self-similarity. They mitigate this difficulty by giving instead data for

$$\frac{\mathrm{d}h_2}{\mathrm{d}t}\left(\frac{\mathrm{d}h_1}{\mathrm{d}t}\right)^{-1} \tag{7}$$

which is calculated as the ratio of slopes in Fig. 10(b) and equals h_2/h_1 at late stages in the self-similarity. In Section 4 the calculated results are shown to lie a bit low for a nonlocal source and a bit high for a local source when compared with the data.

Self-similarity in our case means that the spreading of the TMZ can be characterized by

$$h_1 = \frac{\alpha(\rho_2 - \rho_1)gt^2}{(\rho_1 + \rho_2)} = \alpha X \tag{8}$$

This expression for the height of the bubble envelope was empirically formulated from experiments by Read (1984) and Youngs (1989). There is experimental uncertainty to the value of the coefficient, α, with quoted values anywhere from 0.02 to 0.3 and greater. Nikiforov (personal communication, 1994) speculates that the large range reflects the effects of miscibility of the fluids. For immiscible fluids there seems to be a fairly broad consensus that $\alpha = 0.065 \pm 0.01$. Our calculated value, $\alpha = 0.079$, is slightly higher than the currently accepted range.

An issue of some interest for our spectral equations is the rate of return to isotropy. Because the process is nonlocal in wave-number space and a thorough investigation is beyond the scope of this study, we have not examined the process in detail. One point that can be mentioned is illustrated in Fig. 11, which shows the degree of anisotropy in the base-case calculation. As plotted versus wave number, R_{nn} and R_{yy} look nearly the same, whereas the spectrally integrated quantities plotted as a function of y demonstrate that there is a significant difference between the two quantities. Note that if $R_{yy} = R_{nn}$, then $R_{xx} = R_{zz} = 0$, and the behavior is completely anisotropic; the interpenetration is entirely "ordered". If $R_{yy} = R_{nn}/3$, then the three diagonal components of the Reynolds stress are equal, and the configuration is completely isotropic ("disordered"). At low wave numbers the former condition prevails; at high wave numbers the complete isotropy is approached. Thus the turbulence is created at low wave numbers in primarily anisotropic (ordered) forms and becomes progressively more disordered at any fixed wave number as the TMZ grows and the spectrum shifts to the left. Interpenetration at the large scales (low wave numbers) is thus predominantly wave-like (hyperbolic, as in multifield flow), whereas at the finer scales (high wave numbers) the interpenetration becomes predominantly diffusive (parabolic, as in the more classical circumstances of "turbulence").

We now describe some calculations that depart in one or another respect from the base case. In the first of these variants, we investigated the consequences of blocking the cascade flux of b at a high wave number. Spectral integrals of b are shown in Fig. 12. With zero spectral flux, the cascade flux is conservative, and the integral now includes the passive parts of the spectrum that pile up at large wave numbers. The representation is a crude approximation of the behavior that would be expected from the presence of a smallest attainable scale, corresponding to a particle size that is not further subdividable. Whereas the C_{fb} term describes an inverse transfer to progressively larger scales, the cascade to small scales shows turbulence effects in tearing down the clumps. With a large Schmidt number, the latter process would be expected to lead to the k^{-1} spectral behavior of a passive scalar for those clump

scales whose wave numbers exceed the viscous cutoff. We have not investigated such circumstances. All of these considerations require an extensive program of investigation that lies far beyond the scope of this article. Fig. 12 shows that the added contribution to the spectral integral is noticeable, especially for the spatial positions (near the original interface) for which direct cascade has been proceeding long enough for a high wave-number buildup. The most significant feature of this calculation is the negligible effect of blockage on the rest of the variables, not shown here because the differences are simply not visible on the plots. Thus the concept of a passive part for the b spectrum is embodied; in that range of wave numbers the creation of a_y is essentially balanced by the large drag of the small-scale clumps, in a range of a_y that is in any case so small (from $k^{-7/3}$ scaling) that its effect is negligible. The configurational value of b in Fig. 12 is given by Besnard et al. (1992) as

$$\frac{\alpha_1\alpha_2(\rho_1-\rho_2)^2}{\rho_1\rho_2}$$

The transported values of b follow the configurational form rather closely, being less near the center and somewhat higher in the lateral regions of the TMZ, principally as a result of diffusion in the transport equation, which is conservative in physical space. Some implementations of single-point turbulence transport equations (e.g. the model of Besnard et al., 1992) into computer codes use a purely configurational form for $b(y,t)$, and our results are consistent with that procedure. Having demonstrated the close relationship between transported $b(y,t)$ and configurational $b(y,t)$, we wonder why not use purely the configurational form. The answer is in two parts. First, there is no configurational form for spectral b, for which the distribution across wave-number space is needed for the spectral analysis, and second, in the presence of phase transitions or molecular diffusion between the two fluids, the transport equation can be directly modified to include these effects, together with the resulting decay of spectral b ultimately to zero. In the examples described here, however, we have assumed that the rate of these extra processes is zero, so that $C_{db} = 0$.

With a sudden complete reversal of the body-force acceleration (e.g. from $g = -1$ to $g = +1$), the zone is expected to de-mix back to its original state with a sharp interface. As pointed out by Nikiforov (personal communication, 1994), single-point transport equations in a finite difference implementation have difficulty in calculating this process. We confirm that difficulty and have identified one aspect of the problem. De-mixing is highly dissipative of energy. In contrast to mixing, in which clumps of a material do not collide with others of the same material, de-mixing is highly collisional within the field of each material. The inelastic collisions involve more detailed microphysics than our current model contains, in particular splash with possible entrainment of the other material. Two-field models calculate de-mixing with deceptive ease in the circumstance of no splash (the "splat-and-stick" limit). When θ_1 or θ_2 has increased back to 1.0, the calculation holds the volume fraction constant thereafter, the incompressibility condition for that field ensures that the velocity comes at once to rest, thereby accomplishing a continuous dissipation of collisional energy as each fluid returns to its pure state. This matter is discussed more extensively by Steinkamp (1996) for the two-field calculations in this limiting mode of de-mix representation.

3. Numerical results for a rapid transient

We have not yet investigated the possible inelastic collisional interactions within a fluid and their appropriate dissipative representation. The issue of particular concern to our developments is the question of self-similarity during the rapid-transient phase of turnaround induced by acceleration reversal. The principle issue concerns the variations of a_y. The other variables, b, R_{nn} and R_{yy} have much smaller transient response. With the reversal of acceleration, there is likewise an instantaneous reversal of $\nabla\bar{p}$. The differential acceleration driver to a_y thus reverses; for a brief period of adjustment that term works in concert with the drag terms towards reversal of the sign of a_y; in this regard the entire spectrum of b becomes active. For the acceleration stage, the pressure and density gradient terms in Fig. 13(a) balance the drag terms at high wave numbers, resulting in negligible changes in a_y, vanishingly small $\partial a_y/\partial t$. Immediately after the acceleration reversal at $t = 65$, the pressure gradient term changes sign, resulting in a relatively larger change of a_y for the high wave numbers. In this respect we say that the high wave number portion of the b spectrum has changed from passive to active.

When a_y reverses sign, the mass flux becomes counter-gradient to the density variation; the two driver terms in the evolution equation for a_y now work in opposition to one other. To further illustrate this point, we see that the pressure gradient term and the density gradient term both counter the drag terms in Fig. 13(a), whereas in Fig. 13(b), immediately following the acceleration reversal, the density gradient term counters not only the two drag terms, but also the pressure term. (As pointed out by Youngs (personal communication, 1993), this opposition is necessary for describing his de-mixing experiments: differential acceleration works to compact the zone whereas density-gradient turbulence flux tends to preserve its dispersal.)

Although the brief opposition of a_y and $\nabla\bar{p}$ during the slowdown parts of turnaround give a negative source to the components of R_{ij}, the net effect is small. For the calculation of turnaround results, we used the spectrally blocked version of the base-case conditions described for Fig. 12, allowed the attainment of self-similar mixing, reversed g (from -1 to $+1$) at $t = 65$, and recorded the turnaround until its more-or-less completion at $t = 80$. The transient

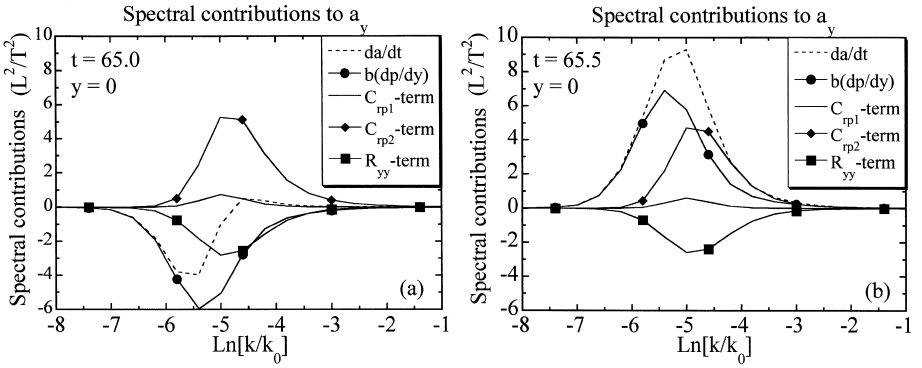

Fig. 13. Spectral contributions of the dominant sources and sinks to the a_y equation for: (a) mixing ($g = -1$), and (b) demixing, immediately after acceleration reversal ($g = 1$).

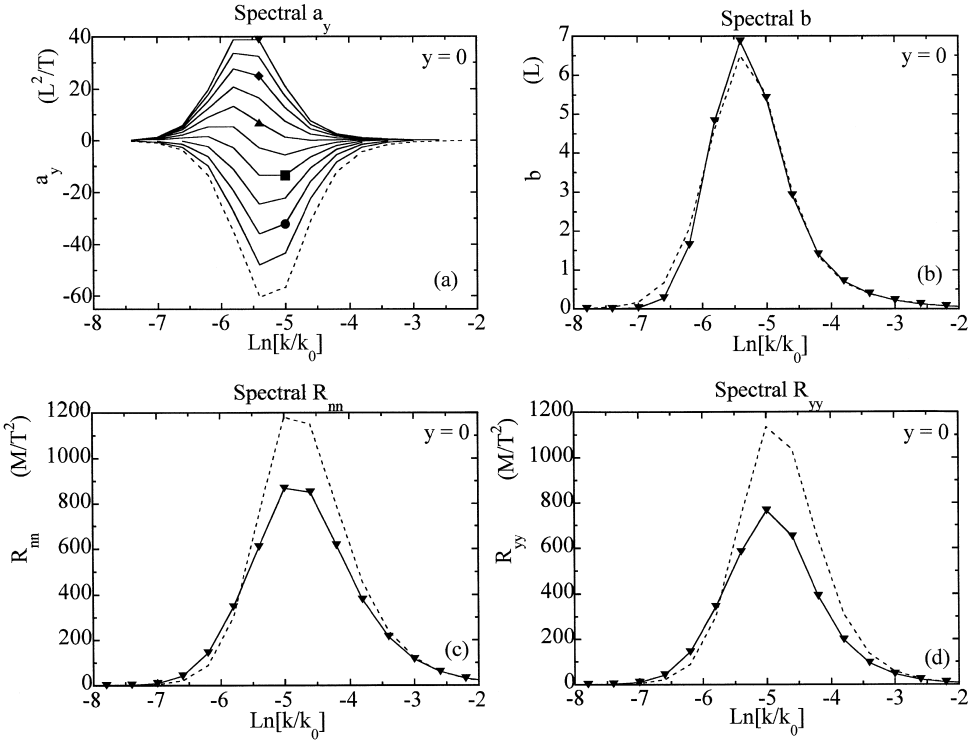

Fig. 14. Spectra at times $t = 65$ (dotted line) and $t = 80$ (upside-down triangles), at the position of the initial fluid interface, for: (a) the net mass-flux velocity, a_y (also including plots for $t = 66.5$, 68.0 (circles), 69.5, 71.0 (squares), 72.5, 74.0 (triangles), 75.5, 77.0 (diamonds), and 78.5); (b) the specific volume–density correlation, b; (c) the contraction of the Reynolds stress tensor, R_{nn} and (d) the R_{yy} component of the Reynolds stress tensor.

phases of structure for a_y are shown in Fig. 14(a). There is a clear departure from the self-similarity during the process. The large scales (small wave numbers) exhibit a more immediate response than the small scales (at large wave numbers). A simple amplitude-modulated function with slowly shifting position in k-space for its maximum is not strictly what occurs; although, in effect, single-point model equations assume this.

Fig. 15 shows that, although the de-mixing process that follows flow reversal cannot be self-similar, the spectral forms as shown in Fig. 15 return to almost precisely those that were present before the acceleration reversal. The implications are important for moment-integral derivations of single-point transport equations: almost-universal forms occur in much wider circumstances than just those that are self-similar.

Variations of spectrally integrated quantities across the TMZ are illustrated in Fig. 16. Fig. 16(a) shows that the heavier clumps of fluid respond more quickly to gravity reversal than the light clumps. The most startling observation is in Fig. 16(b), which shows negative values of b where the heavier fluid is falling back into itself.

The anomaly is also seen in Fig. 17, in which the average density exceeds 2.0 at this fall-back locality. In the two-field calculations of Steinkamp (1996), this impossibility is avoided by the dissipative technique described above for one possible type of mixing. The same "stick-and-splat"

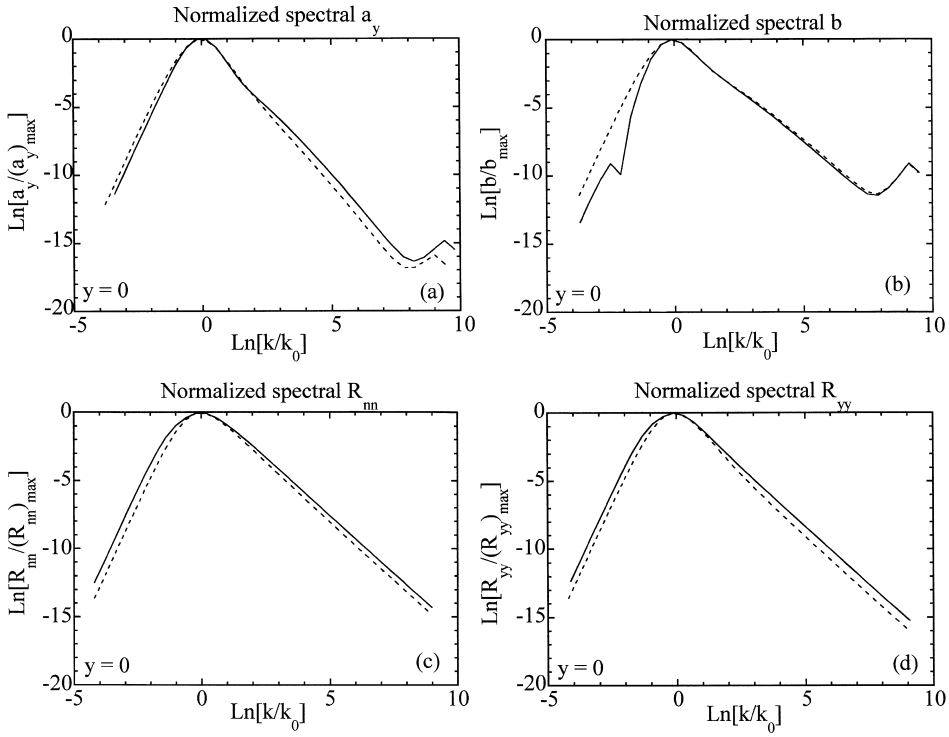

Fig. 15. Normalized spectra for $t = 65$ (dotted line) and $t = 80$ (solid line), at the position of the initial fluid interface, for: (a) the net mass-flux velocity, a_y; (b) the specific volume–density correlation, b; (c) the contraction of the Reynolds stress tensor, R_{nn} and (d) the R_{yy} component of the Reynolds stress tensor.

fix technique could also be employed here, but the topic requires extensive consideration and discussion for more general de-mixing circumstances, which is beyond the scope of this article.

The base case calculation without spectral blockage was also performed for the mixing of two fluids with a larger density ratio, $\rho_2/\rho_1 = 5.0$. The results exhibit essentially the same attainment of self-similarity, with spectral exponents corresponding to those in Fig. 2.

For the case with a density ratio of 5.0, as in Fig. 3, the ordering of exponent values in Table 1 for low wave numbers is the same and for the same reasons having to do with the effects of C_{fb}. For high wave numbers we see again the large contrast between the cascade-dominated behavior of R_{ij} and b, for which $m \approx -5/3$ and the drag-dominated behavior of a_y,

Table 1
Power law behavior for both the low and high wave numbers for the transported spectral variables

Quantity	Low-k exponent	High-k exponent
$R_{ij}(k)$	3.99	−1.74
$b(k)$	3.87	−1.71
$a_y(k)$	3.92	−2.37

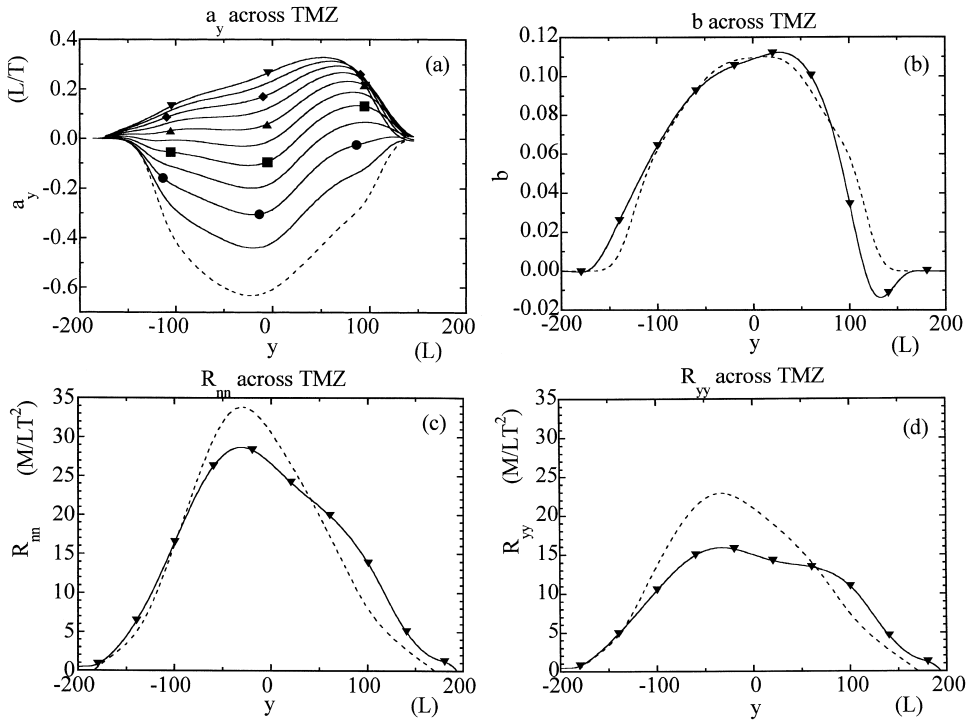

Fig. 16. Profiles of spectrally integrated variables across the TMZ for $t = 65$ (dotted line) and $t = 80$ (upside-down triangles) of (a) the net mass-flux velocity, a_y (including plots for $t = 66.5$, 68.0 (circles), 69.5, 71.0 (squares), 72.5, 74.0 (triangles), 75.5, 77.0 (diamonds) and 78.5); (b) the specific volume–density correlation, b; (c) the contraction of the Reynolds stress tensor, R_{nn} and (d) the R_{yy} component of the Reynolds stress tensor.

for which $m \approx -7/3$. The value of α, the self-similar growth coefficient for h_1, is 0.11, which is appreciably larger than either the base-case result or the experimentally observed result. In addition, h_2/h_1 approaches the magnitude 1.08, which is low.

4. Local versus nonlocal source term

Two intriguing disagreements with experiments are especially noticeable in the results discussed so far (see Table 2). One is the coefficient for self-similar growth of h_1, which is

Table 2
Self-similar coefficient, α, and the asymmetry of the TMZ for the two numerical runs and experiments

Source to R_{ij}	α	h_2/h_1
Local	0.042	1.79
Nonlocal	0.079	1.05
Experiments	~0.065	~1.30

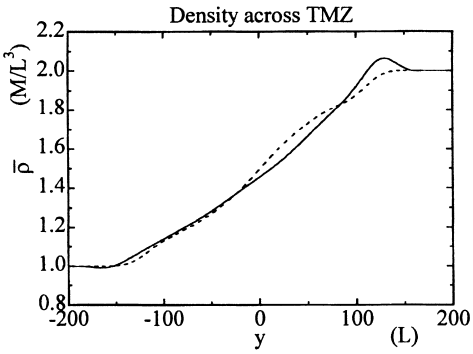

Fig. 17. Profiles of density across the TMZ for $t = 65$ (dotted line) and $t = 80$ (solid line).

somewhat too large, and the other is the asymptotic ratio of h_2/h_1, which is too small. An intriguing clue to remediation of both discrepancies lies in the results described by Figs. 18–22. In those figures we compare the base case with local and nonlocal source terms for R_{nn} and R_{yy}. Fig. 18 shows the large contrast in results. With the local source, density exhibits sharp variations on each side of the TMZ; these are more spread out with the nonlocal source.

The coefficient, α, is sharply reduced to the value $\alpha = 0.042$, whereas the ratio of penetration depths, h_2/h_1, approaches the much larger value of 1.79. In both respects the experimental values lie between the extremes.

It thus appears that a more restrictive nonlocal formulation for $Q(y',y)$ could produce closer agreement with experiments in both respects. The task of deriving such a formulation remains a challenge yet to be addressed.

The spectral behaviors are compared at low and high wave numbers in Figs. 19 and 20. At the low wave numbers, there is a significant effect, which is discussed in Appendix C of Article I. At the high wave numbers there is very little difference between the local and nonlocal formulations. Here we merely observe that the spectrally preserving local source is structurally dominated by the C_{fb} effects, so that the exponent is lower than with the nonlocal source, which is not spectrally preserving and indeed tends to increase the exponent at low wave numbers. This complicated set of interactions is discussed in more detail in Article I.

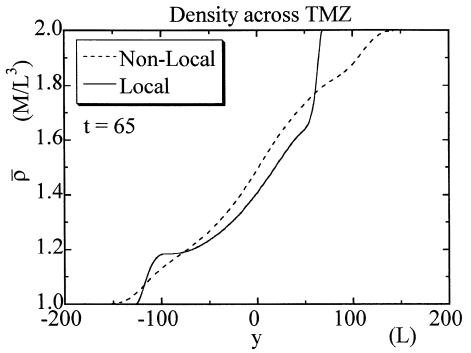

Fig. 18. Comparison of the density across the TMZ for a local source to R_{ij} and a nonlocal source to R_{ij}.

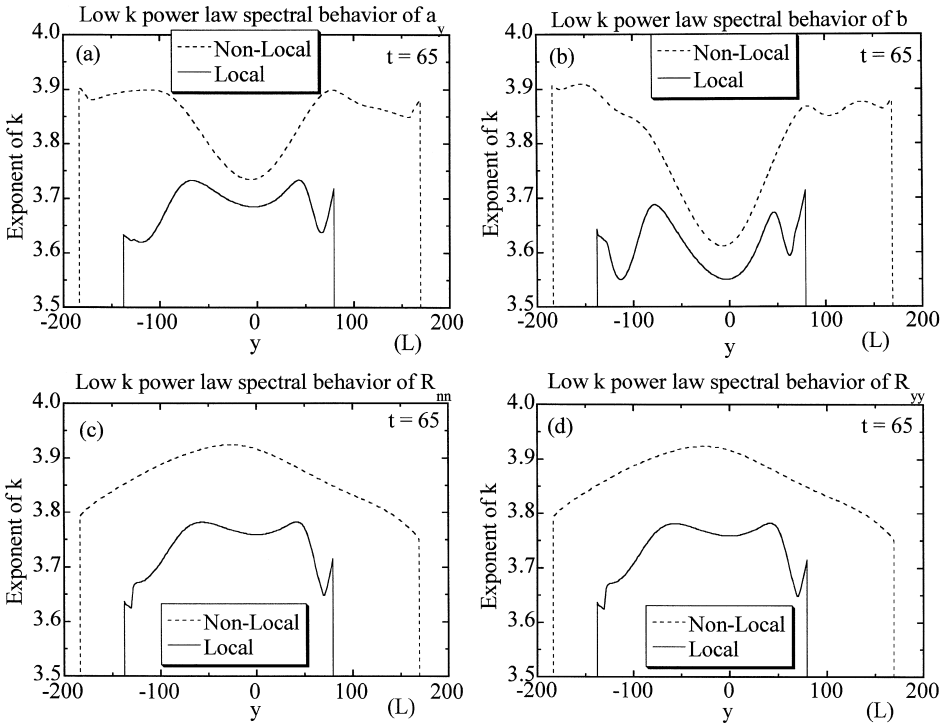

Fig. 19. Comparison of the low wave number, power-law behavior of k at $t = 65$ for a local and nonlocal source term: (a) the net mass-flux velocity, a_y; (b) the specific volume–density correlation, b; (c) the contraction of the Reynolds stress tensor, R_{nn} and (d) the R_{yy} component of the Reynolds stress tensor.

Fig. 21 is comparable to Fig. 4, with both showing the evolution towards self-similarity at a distance of 50 units below the original interface. The results are quite similar; in both cases the first influence to arrive is that of a_y, which tends to impart $k^{-7/3}$ behavior at the high wave numbers, soon to be dominated, however, by the effects of cascade that convert the spectrum to $k^{-5/3}$. At the lower wave numbers the spectrum arrives in completely self-similar form.

The contrast between local and nonlocal lateral propagation is manifested in slightly less departure from self-similarity at high wave numbers in the local case, especially in the spectra of R_{nn} and R_{yy}. The reason is that nonlocal propagation favors more rapid lateral distribution of the larger scales, with corresponding slower lateral distribution of the smaller scales.

This difference in lateral propagation is especially apparent in Fig. 22, which shows the spatial distributions of scale lengths (reciprocals of wave numbers for the spectral extremum) at a late time in self-similar TMZ growth. Disregarding structural details in the profiles, we notice a significant difference between the local and nonlocal results. For the local source term, the length scales all tend to decrease towards the edges of the TMZ. With a nonlocal source term, the profiles for a_y and b are essentially the same, whereas for R_{nn} and R_{yy} the scales increase significantly towards the edges. It is this feature that especially demonstrates the desired consistency with Rayleigh–Taylor theory, as discussed in Appendix A of Article I.

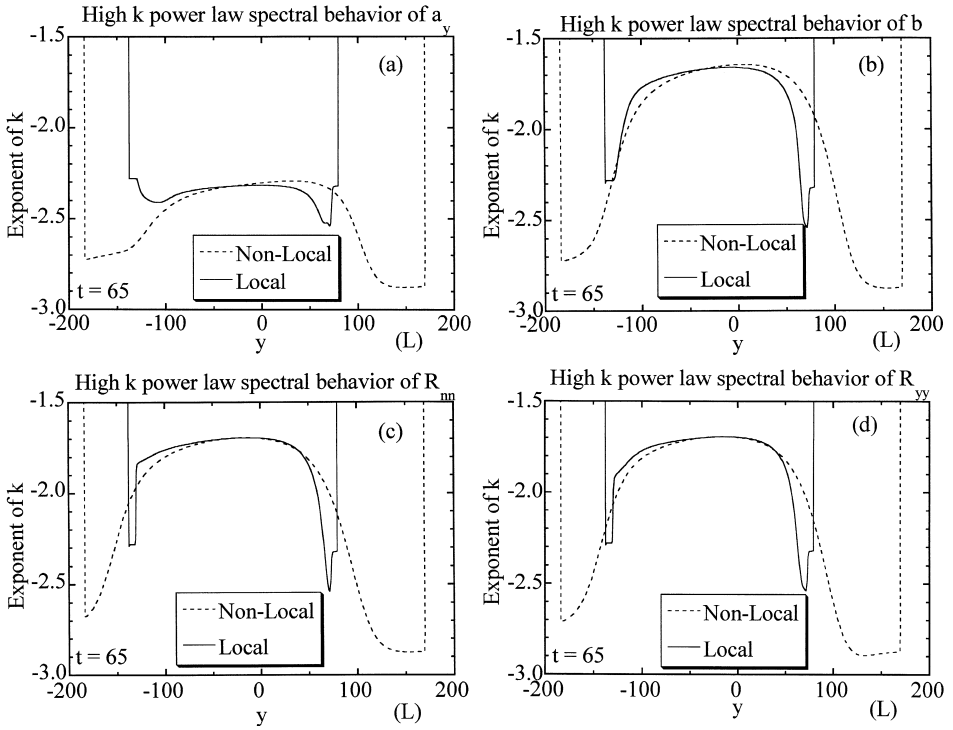

Fig. 20. Comparison of the high wave number, power-law behavior of k at $t = 65$ for a local and nonlocal source term: (a) the net mass-flux velocity, a_y; (b) the specific volume–density correlation, b; (c) the contraction of the Reynolds stress tensor, R_{nn} and (d) the R_{yy} component of the Reynolds stress tensor.

The issue of $\bar{\rho}$ variations across the TMZ can be put into clearer perspective by further consideration of the experimental observations. Fig. 23 is adapted from the Russian report (Kucherenko et al., 1991) in which they analyze the process for a variety of different density ratios, $n = \rho_2/\rho_1$. The principal issue concerns the identification of edge locations for the TMZ for which they use both photographic and X-ray techniques. They define edge positions in terms of a fractional quantity, δ, which designates fraction of purity for the heavier fluid at which the edge is defined to be located. Typical values are $\delta = 0.10$, 0.90 and $\delta = 0.01$, 0.99 (this last being stated as 0.98 on one of the Fig.s in their report, presumably erroneously).

Fig. 23(a) shows variations in the average fluid density across the TMZ for a typical example, $n = 3$. Error bars indicate the uncertainty, especially with implications for edge location. With $\delta = 0.01$, 0.99, the distances h_1, and especially h_2 depend strongly on how the datum points are connected through the envelope of error bars. With $\delta = 0.10$, 0.90, the sensitivity is reduced, and the ratio, h_2/h_1, is considerably smaller. Fig. 23(b) and (c) illustrates the effects of choosing different edge criteria. Combining both Russian and British data, we see in Fig. 23(d) a considerable scatter in data. The figure also shows the base-case numerical results for both the local and nonlocal sources, as well as the case of a density ratio, n, of 5 using a nonlocal source term (as previously discussed in Section 3 of this paper). Numerical

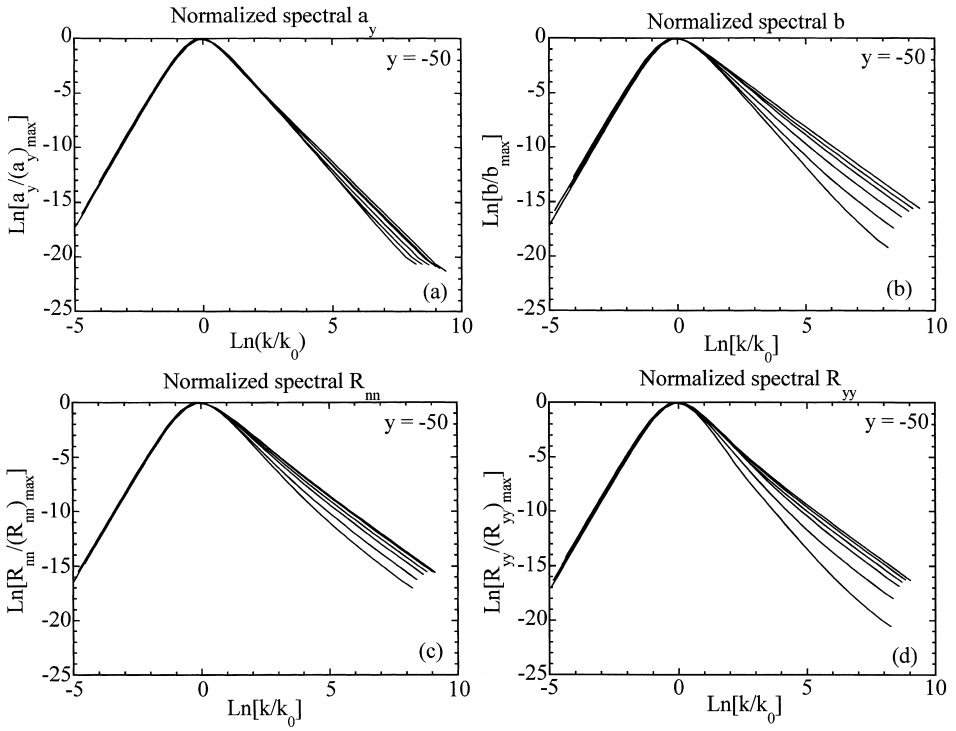

Fig. 21. Normalized spectra for $t = 30$, 35, 40, 45, 50, 55, 60 and 65, a distance of 50 units of length below the centerline of the TMZ for: (a) the net mass-flux velocity, a_y; (b) the specific volume–density correlation, b; (c) the contraction of the Reynolds stress tensor, R_{nn} and (d) the R_{yy} component of the Reynolds stress tensor.

problems have precluded testing the model for density ratios greater than 5. Refer to Table 2 for the values of h_2/h_1.

The calculation with the nonlocal source is considerably closer to the most-likely experimental value, but it is apparent that more precise data would be useful as a basis for validation of any modified form for $Q(y',y)$ in the expression for nonlocal creation.

Subsequently, a calculation was performed for a somewhat different departure from the base case, to examine the consequences of modifying the low wave number initialization of b. In the initial-condition formula for b in the interface computational cell, Eq. (1), we used $m = 4$ in the base case and $m = 2$ in this modified run.

Here γ_1 and γ_2 are specified by Eq. (3). All other conditions were the same for the two calculations. The purpose for the comparison is to explore the possibility of nonuniqueness for late-time self-similarity as induced by the persistence of structure at low wave numbers, i.e. the persistence of memory of large scales. This intriguing question has been discussed at length by previous investigators. Constant density, isotropic turbulence has been analyzed by a number of investigators using the EDQNM model; Lesieur and Schertzer (1978) show that for m greater than or equal to 4, a single self-similar form function will emerge; for $m < 4$, spectra will persistently depend on the value of m. In fully three-dimensional **k**-space the continued influence of low wave-number structure on self-similarity gives a rich set of potential form

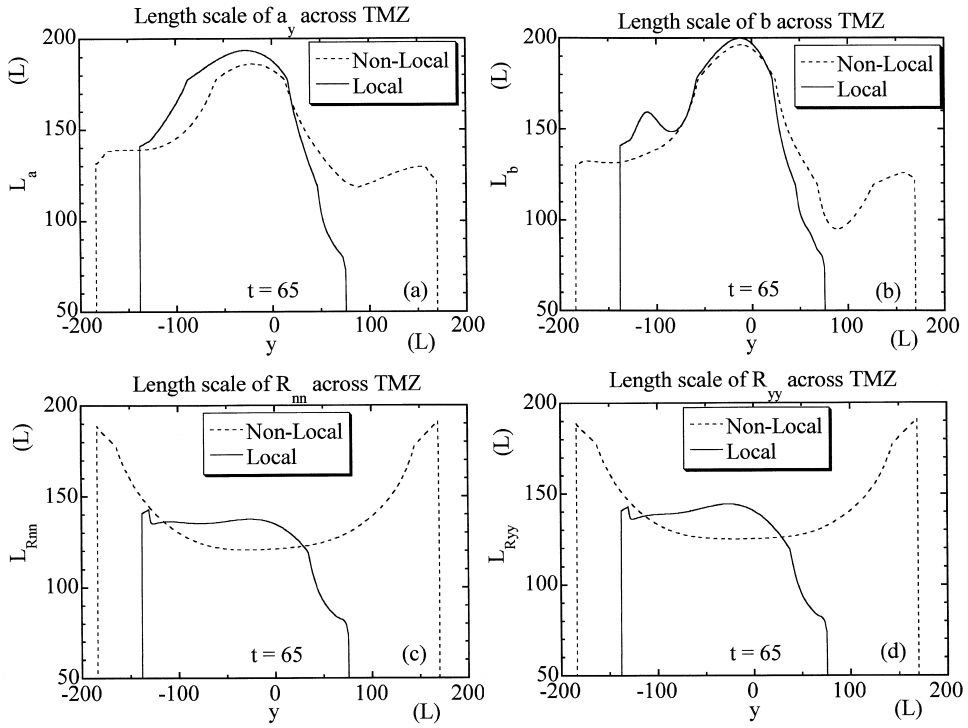

Fig. 22. Comparison of the profiles of the length scales across the TMZ for a local and nonlocal source term at $t = 65$ for: (a) the net mass-flux velocity, a_y; (b) the specific volume–density correlation, b; (c) the contraction of the Reynolds stress tensor, R_{nn} and (d) the R_{yy} component of the Reynolds stress tensor.

functions. In the current comparison we see that with $m = 2$ the differences from the base-case results are so slight, largely due to choice of modeling, that we could not effectively illustrate them in figures.

With $m = 2$

- the values of a_y, R_{nn} and R_{yy} are slightly larger;
- h_2/h_1 is slightly smaller (asymptotically, $h_2/h_1 \approx 1.03$);
- the TMZ spreads a bit faster, $\alpha = 0.098$;
- the spectra all propagate slightly faster toward low wave numbers.

These trends are qualitatively consistent with the fact that $m = 2$ gives larger b values for small wave numbers, persistently resulting in creation enhancement for a_y and in turn the Reynolds-stress components.

As a last numerical example, we discuss the effects that result from a change in C_{fb}, the "bubble-doubling" coefficient. In the base case, $C_{\mathrm{fb}} = 0.50$; in the comparison calculation C_{fb} is increased to 0.65. The most prominent of the results are shown in Fig. 24. As discussed in Appendix C of Article I, there are competing processes at low wave numbers, for which the three most prominent contributors are

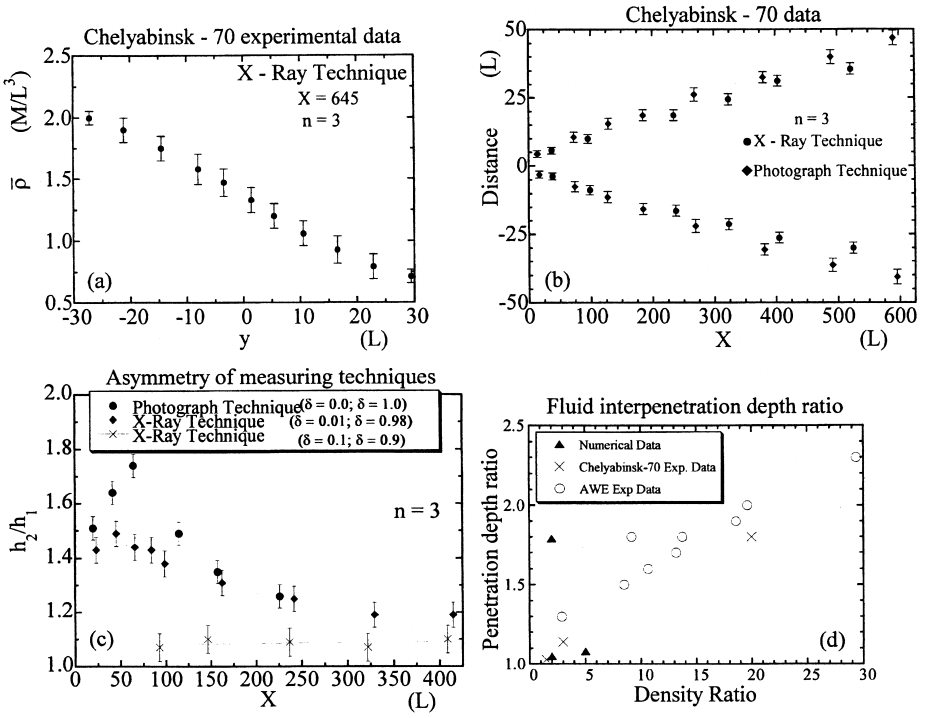

Fig. 23. Experimental data from Chelyabinsk-70 (Kucherenko et al., 1991) for: (a) concentration profile through TMZ ($n = 3$); (b) bubble and spike penetration depth; (c) asymmetry of spike to bubble ratio and (d) comparison of numerical results to experiments (Kucherenko et al., 1991; Smeeton and Youngs, 1987).

- the initialization exponent, m, for b;
- the value of C_{fb};
- the nonlocal source for Reynolds stress.

The dominant effect is that of m, which sets the exponent for all the variables to magnitudes not far from m and that persist into the self-similar stages. Nonlocality of source to Reynolds stress tends to increase the exponent; only the local source is spectral-form preserving (i.e. imparts the low wave-numbers form of a_y without distortion). The C_{fb} contribution tends to decrease the exponent at low wave numbers for b, with the effect spreading to a_y and thence to R_{nn} and R_{yy}. The net effect of these influences is seen in Fig. 24, which shows the greatest change in b, less in a_y, and even less in the Reynolds-stress spectra. Also apparent in Fig. 24 is the greater width of the TMZ for the calculation with larger C_{fb}. At high wave numbers the effects of this increase in C_{fb} are negligible. Comparisons of self-similar spectral forms are not illustrated in the figures; the forms are almost precisely the same as for the base case; with $C_{\mathrm{fb}} = 0.65$ all of the normalized spectral forms show slightly higher magnitudes at low wave numbers and slightly lower magnitudes at high wave numbers.

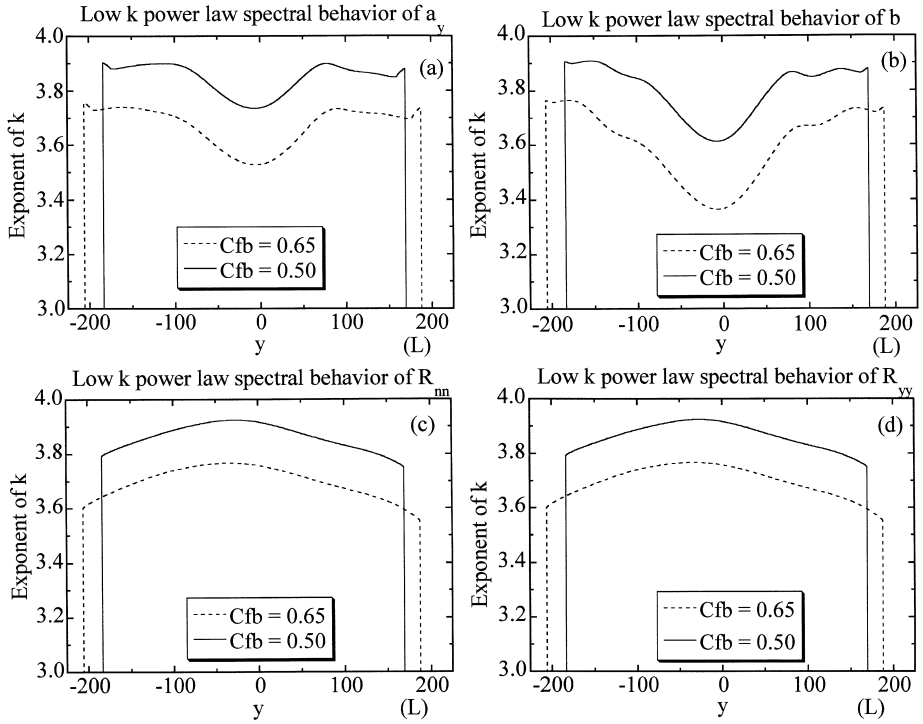

Fig. 24. Comparison of the low wave number, power-law behavior of k at $t = 65$ for two different values of C_{fb} for: (a) the net mass-flux velocity, a_y; (b) the specific volume–density correlation, b; (c) the contraction of the Reynolds stress tensor, R_{nn} and (d) the R_{yy} component of the Reynolds stress tensor.

5. Conclusions

A spectral turbulence transport model for variable density flows has been formulated (Article I) and applied to a turbulent mixing layer. Comparisons with experiment indicate that our model is capable of capturing the evolution of the self-similar stage of mixing that ensues from the Rayleigh–Taylor instability. In addition to matching the available experimental data on Rayleigh–Taylor instabilities, the formulation provides much more meaningful physical insight into the structure of the turbulence beyond that which single-point models are capable of providing. Examples are also given for a case of acceleration reversal to demonstrate the spectral behavior throughout a rapid transient in the mean flow driver.

The spectral model also allows the development of a systematic way to incorporate increased sophistication into a single-point model through spectral integration. As a result, development of single-point models that includes more physics than the current single-point models may be possible. This technique provides a basis for determining when a single-point model is adequate to describe a flow (i.e. the flow is in spectral equilibrium) and when we are forced to resort to the more expensive spectral model (i.e. the flow is out of spectral equilibrium due to rapid transients in the mean flow drivers). When the flow is in spectral equilibrium, the length scales maintain a constant ratio, and the single-point models are adequate for describing the

flow, but when the flow experiences a transient, the length scales fluctuate relative to one another, and a spectral model is needed to describe the flow until it has once again returned to spectral equilibrium. A spectral model permits the investigation of this rate of return to equilibrium and identifies the primary competing processes responsible for these rates, such as mean flow time scales versus cascade and decay time scales.

This spectral model has enabled us to identify spectral self-similarity in the mixing of two fluids for the first time. It has been known for some time, both experimentally and numerically, that the turbulent mixing due to the late stages of the Rayleigh–Taylor instability is a self-similar process. This model has, for the first time, allowed us to examine the spectral relations between the various components of the flow and gain insight into the approach to self-similarity, and consequently the realm of validity for the single-point models. We have identified independent self-similar behavior for both k-space and physical space.

To complement the previous research in spectral turbulence transport modeling, this research has made three significant contributions: (1) a nonlocal source term for the Reynolds stress transport equation that accounts for the global pressure effects due to incompressibility; (2) a source term to the b equation driven by the density-gradient that contributes to the "bubble doubling" phenomena of turbulent structures as observed by experiment; and (3) a configurational source term to the b equation that is rigorously derived for the two-fluid circumstance. All three of these contributions result in significant improvements to the spectral model.

This spectral model provides the physical fidelity, above and beyond that given by single-point transport models, for the improved modeling of flows that are aligned with real life situations. The spectral model thus allows for the description of flows that undergo rapid transients, and, hence, may be useful in a variety of practical applications.

Acknowledgements

We are very grateful to Margaret Findley of the Fluid Dynamics Group, T-3, for helping to design and prepare this manuscript. This work was performed at Los Alamos National Laboratory, which is operated by the University of California under the auspices of the United States Department of Energy (contract W-7405-ENG-36).

Appendix A

A.1. Self-similar forms

In this article we have demonstrated the concept of statistical self-similarity for the example of a TMZ between two immiscible fluids. As an idealization, the zone extends laterally in all directions and all quantities are statistically independent of the lateral dimensions. Indeed, we have assumed that ensemble averaging can be replaced by lateral spatial averaging, with results

that vary in time only as functions of wave number and the distance normal to the layer. Such an idealization does not exist in nature, but there are nevertheless numerous circumstances in which it serves as a good approximation.

Jeandel et al. (1978) argued that statistical self-similarity is a crucial element for the validity of single-point turbulence transport models. In order to describe with a small number of variables the collective effects of a virtually infinite number of degrees of freedom, it is clear that severe constraints must exist to confine the dynamics of the fluid to a very small set of all possibilities. Moreover, one of the necessities for single-point applicability is that the return to self-similarity occurs rapidly after a change in the external drive conditions.

Self-similarity of the statistics is characterized by self-similar statistical forms. They always occur with the same structure for a specific set of mean flow circumstances after proper space- and time-scalings are performed. ''Universal'' self-similar forms, however, are idealizations that never precisely occur in nature, although in many situations of interest they may be approximately satisfied. The forms of such functions may strongly reflect the existence of anisotropy and may depend on persisting conditions in the limit as $|\mathbf{k}| \to 0$. Subsets can be found in k or y space alone and in various other combinations of the wave number and position-vector components. Complete analytical derivation is difficult (see Besnard et al., 1996); partial derivations are well known for simple cases (e.g. the $k^{-5/3}$ inertial range for $R_{\alpha\alpha}$; more general extraction may only be possible numerically).

The simplest statistical self-similar forms occur in the decay of homogeneous isotropic turbulence for constant density fluid with vanishing viscosity. Besnard et al. (1996) discuss this form and use an anisotropic generalization to derive spectral moments. They show that with this simple idealization, the single-point equations (e.g. K–ε models) can be derived. These types of single-point equations have been successfully applied to circumstances far beyond the case of homogeneous anisotropic decay.

In general, self-similarity for the behavior of some turbulence statistic like $R_{ij}(y,k,t)$ (we have included the arguments in this appendix for clarity) means that a scaling law can be found for its variations in magnitude, such that the scaled quantity is then a function only of the combined variables, $y/L(t)$ and $kL(t)$, in which $L(t)$ is a function with the dimensions of length. Thus the function of three variables, y, k and t, has been transformed to a function of two variables.

This scaling of magnitudes and the independent variables that define self-similarity can be described more precisely. Consider the behavior of

$$E(y,k,t) = \frac{1}{2\rho} R_{nn}(y,k,t) \tag{A1}$$

which has the dimensions of $(distance)^3/(time)^2$. Suppose we scale the space and time coordinates such that

$$y \to \omega^n y$$

$$k \to \omega^{-n} k$$

$$t \to \omega^m t \tag{A2}$$

where ω is a dimensionless number that defines the scale, while m and n are numbers to be specified. We also scale the magnitude of E according to its dimensionality,

$$E \to \omega^{3n-2m} E \tag{A3}$$

Our constraint of self-similarity in this process results in the equation

$$\omega^{3n-2m} E(k, y, t) = E(\omega^n y, \omega^{-n} k, \omega^m t) \tag{A4}$$

Differentiate with respect to ω and then set $\omega = 1$. The result is

$$(3n - 2m)E = ny\frac{\partial E}{\partial y} - nk\frac{\partial E}{\partial k} + mt\frac{\partial E}{\partial t} \tag{A5}$$

that can be solved to give

$$E(y, k, t) = t^{\frac{3n-2m}{m}} \hat{F}\left[\frac{y}{t^{n/m}}, kt^{n/m}\right] \tag{A6}$$

where $\hat{F}$ is an arbitrary function of its arguments. The origin of time is arbitrary, so that we may choose the onset of self-similarity at some time, t_0, and write

$$L(t) \equiv L_0(t - t_0)^{n/m}$$

$$K(t)L(t) \equiv K_0 L_0 (t - t_0)^{\frac{3n-2m}{n}} \tag{A7}$$

thus re-expressing the solution in the form

$$E(y, k, t) = K(t)L(t)F\left[\frac{y}{L(t)}, kL(t)\right] \tag{A8}$$

with F having absorbed some constants and likewise being an arbitrary function of its arguments. Note that in this form

$$\int_0^\infty E(y, k, t)\mathrm{d}k = K(t)G\left(\frac{y}{L(t)}\right) \tag{A9}$$

where

$$G(\eta) \equiv \int_0^\infty F(\eta, \xi)\mathrm{d}\eta. \tag{A10}$$

This form for $E(y,k,t)$ describes a constraint of self-similarity. It is derived without reference to

the transport equation for E and serves to distinguish from all possible solutions a particular subset with a type of self-similarity.

Dimensional arguments for the spectrally integrated quantities are based on the TMZ growth having "forgotten" all finite scale details of the initial conditions so that the acceleration g is the only dimensional scaling parameter. Thus any velocity scale must vary as gt while the turbulence energy per unit mass and length scales vary as gt^2. Thus n and m are constrained to $n = 2m$.

Applied to homogeneous, isotropic turbulence, the result of self-similarity is the conversion of a partial differential equation for $E(k,t)$ to an ordinary differential equation for $F[kL(t)]$. Besnard et al. (1996) discuss in detail the properties of F.

For the mixing-layer analysis in y–k space, the self-similarity constraint has likewise reduced the number of independent variables, but insertion into the transport equation nevertheless results in a partial differential equation for $F(y/L,kL)$, which has a much greater richness of possible solutions than the ordinary differential equation for homogeneous, isotropic circumstances. We thus see hints of possible nonuniqueness of self-similar mixing-layer turbulence.

The breadth of possibilities increases substantially when we examine the behavior in six-dimensional circumstances. Recognizing the dimensionality of $R_{ij}(\mathbf{x},\mathbf{k},t)/2\rho$ as $(distance)^5/(time)^2$, we can derive a self-similar constraint in the form

$$\frac{R_{ij}(\mathbf{x},\mathbf{k},t)}{2\rho} \equiv K(t)L^3(t)F_{ij}\left[\frac{\mathbf{x}}{L(t)},\mathbf{k}L(t)\right] \tag{A11}$$

where

$$L(t) \equiv L_0(t-t_0)^{n/m}$$

$$K(t)L^3(t) \equiv K_0L_0^3(t-t_0)^{\frac{5n-2m}{m}} \tag{A12}$$

Insertion of this form into the full transport equation reduces the seven independent variables in the partial differential equation to six independent variables. For the mixing layer with physical-space dependence on y, only, the number of independent variables is four. We are in the process of examining some of the properties and consequences of this more general self-similarity for the turbulence of a single fluid with constant density, but such discussions for variable-density fluids are beyond the scope of this article.

We are, however, concerned with extensions to the self-similar form in our special case of the mixing layer. We rewrite Eq. (A8) with a different combination of variables in the F function (which is perfectly allowable) i.e.

$$E(y,k,t) = K(t)L(t)F\left[\frac{y}{L(t)}, kL(t)G\left(\frac{y}{L(t)}\right)\right] \tag{A13}$$

We hypothesize that the G function can be found in such a way that

$$F\left[\frac{y}{L(t)}, kL(t)G\left(\frac{y}{L(t)}\right)\right] = F_1\left(\frac{y}{L(t)}\right)F_2\left[kL(t)G\left(\frac{y}{L(t)}\right)\right] \tag{A14}$$

This hypothesis is capable of being tested numerically. It states in effect that the spectrum is self-similar in k-space with a shift in maximum and position thereof for which $kL(t)$ depends only on η, where $\eta = y/L(t)$. The first realization of this form was described by Besnard et al. (1996) on the basis of numerical solutions of their spectral model equations for a constant-density fluid in a temporally evolving shear layer. In this article we have described a further realization for the turbulent mixing of two fluids.

We are led to define a length scale $L(y,t)$ that varies with both position and time, as was assumed by Besnard et al. (1996) for the spectral-moment derivations of single-point transport equations. Thus we define $L(y,t)$ as being equal to $L(t)G(\eta)$, and $K(y,t)L(y,t)$ as identically being equal to $F_1(\eta)L(t)K(t)$. Then Eqs. (A13) and (A14) can be written as

$$E(y,k,t) = K(y,t)L(y,t)F_2\big[kL(y,t)\big] \tag{A15}$$

Even more generally, if the mixing layer is of finite lateral extent or curved away from planarity, we postulate the concept of localized self-similarity with $K(\mathbf{x},t)$ and $L(\mathbf{x},t)$, which is the actual form used for deriving moment equations for turbulence in a constant density fluid. In this more general case, we believe that the decomposition described in Eqs. (A13) and (A14) is also relevant.

Appendix B

B.1. Moments of the spectral equations

With the spectral transport equations of Article I, it is possible to solve a much wider scope of problems than can be addressed with single-point (nonspectral) formulations. Rapid variations in drive, for example, distort the nearly self-similar form functions into strongly circumstance-dependent expressions. Spectral equations work well for describing such processes, but spectrally integrated moment equations, based on assumed persistence of self-similarity, may exhibit large errors for such applications.

Spectral transport formulations are more complicated, however, as well as being much more expensive to use in numerical investigations with high-speed computers. Thus we use the two

approaches in complementary fashion; in particular, we look at the spectral approach for clues to improving and extending the moment equations.

Steinkamp (1996) discusses the single-point turbulence transport equations in terms of previous nonspectral derivations, to which are added some important clarifications and extensions. Significant difficulties are also described, especially in regard to size scales associated with both the turbulence and the interfacial configuration of mixing fluids. Decay of turbulence, for example, is directly related to the transfer rate from low to high wave numbers. Sources to turbulence can be strong in the "active" scales and weak in the "passive" scales, the latter simply balancing the buoyancy forces with drag. The resolution of these and other questions leads directly to the spectral formulations; the inverse process takes the spectral equations back to single-point form but augmented with representations of the principal spectral improvements that were previously missing.

Before proceeding with the derivations, we describe an example of the new single-point augmentation. For the simple self-similar mixing layer that dominates the considerations of this article, it is arguable that single-point transport equations are not required for both $a_y(y,t)$ and $R_{ij}(y,t)$. They are, after all, scaled in dimensionality by the same quantity, acceleration $\mathbf{g}$; and the spectral functions on which they are based are of universal form, so that knowledge of one implies that the other is known. Moreover, the scales associated with the spectral quantities b, a_y, and all the components of R_{ij} must be directly proportional to each other with universal ratios. Thus a pair of single-point equations for $a_y(y,t)$ and its associated length scale, $L_a(y,t)$, should be sufficient to determine the entire process. These ideas are amply verified in the examples shown in Section 2.

Those examples show, however, that at the moment when self-similarity is destroyed (e.g. through reversal of $\mathbf{g}$), the relationship among a_y, R_{nn} and R_{yy} is at once lost. Each evolves in its own particular response to the new circumstances, returning to a unique, universal relationship to each other only when (and if) self-similarity is again established (which is not the case during the de-mixing process), in which the width of the layer at the instant of acceleration reversal is firmly implanted as an additional dimensional quantity. In addition, the length scales associated with each of the spectra are now no longer universally proportional to each other. If the driver continues to vary in capricious fashion, these independent behaviors continue; and the discernment of relationships among variables requires the simultaneous transport analysis of them all.

The spectral equations describe all these "independent" but interactive behaviors. Can single-point (spectral-moment) equations do likewise? There is evidence to suggest that they can do fairly well in this regard. Simple single-point $R_{ij}(y,t)$–$\varepsilon(y,t)$ models describe at least some types of transient circumstances, despite their derivation being equivalent to moments of the spectral form functions.

At least two things must contribute to the success of single-point (nonspectral) formulations. One of these is the tendency for spectra to vary principally in magnitude during many kinds of

transients, with little change in form (for example, a_y during acceleration reversal in Section 3). The second is the tendency for rapid return to self-similarity after a transient change in drive. This latter, indeed, furnishes a significant criterion for spectral-moment transport validity in terms of the competition between change in rate of drive and return rate to self-similarity. With the spectral equations, this competition can be examined in detail.

In this Appendix we show the spectral moment derivations for the simplest TMZ, in which all ensemble averaged (layer-averaged) spectral quantities are functions of y, k and t only. We write

$$\begin{aligned} a_y(y,k,t) &= a_y(y,t)L_a(y,t)F_a\big(kL_a(y,t)\big) \\ b(y,k,t) &= b(y,t)L_b(y,t)F_b\big(kL_b(y,t)\big) \\ R_{ij}(y,k,t) &= 2\bar{\rho}(y,t)K(y,t)L_R(y,t)F_{ij}\big(kL_R(y,t)\big) \end{aligned} \tag{B1}$$

Here, $K(y,t)$ denotes the single-point turbulent kinetic energy and as usual, $\bar{\rho}(y,t)$ is the average density. The wave number, k, occurs only in the self-similar form functions, the Fs. The purpose of this Appendix is to derive spectral moment equations to describe the transport of $a_y(y,t)$, $b(y,t)$, $K(y,t)$, $L_a(y,t)$, $L_b(y,t)$, and $L_R(y,t)$.

There are an infinite number of possible moments. The spectral-moment transport equations that we propose are six in number, two for each of the spectral equations for a_y, b and R_{nn}, since each has two unknown functions of position and time, a magnitude, and a length scale. (At this stage we assume that the difference between R_{nn} and R_{yy} is sufficiently represented by their two different forms, namely F_{nn} and F_{yy}).

We substitute the self-similar forms of Eq. (B1) into the spectral transport equations of our model, i.e. Eqs. (25), (33) and (35) from Article I and integrate over dk to get evolution equations for $K(y,t)$, $a_y(y,t)$, and $b(y,t)$. The resulting transport equations depend on time and the physical-space variable, y, only. Due to the self-similar forms of Eq. (B1), length scales for each of the variables are incorporated into the new single-point transport equations. These length scales, namely $L_a(y,t)$, $L_b(y,t)$ and $L_R(y,t)$, may be considered the inverse of the dominant wave number $k_{\max}$ of the spectrum for each of the variables. In addition to performing the integrations just described, we also integrate the spectral transport equations over $k^m\mathrm{d}k$ for $m=-1$ to get transport equations relating the single-point quantities to their associated length scales.

The functions are normalized to

$$\int_0^\infty F_a(\xi)\mathrm{d}\xi = \int_0^\infty F_b(\xi)\mathrm{d}\xi = \int_0^\infty F_{nn}(\xi)\mathrm{d}\xi = 1 \tag{B2}$$

The maximum value of all three form functions is unity corresponding to the position $\xi = 1$.

The process of substituting the self-similar forms from Eq. (B1) into the spectral transport equations and performing the integrations discussed above is straightforward. The local cascade terms are the only terms that warrant closer examination. The integration will be shown for the cascade of a generic variable, φ.

The generic cascade terms are expressed as

$$\frac{\partial}{\partial k}\left[k^2\sqrt{\frac{kR_{nn}}{\bar{\rho}}}\left(-C_1\varphi + C_2 k\frac{\partial\varphi}{\partial k}\right)\right] \tag{B3}$$

Taking the mth moment of this cascade term

$$\int_0^\infty k^m \frac{\partial G(k)}{\partial k}\,\mathrm{d}k \tag{B4}$$

where

$$G(k) = k^2\sqrt{\frac{kR_{nn}}{\bar{\rho}}}\left(-C_1\varphi + C_2 k\frac{\partial\varphi}{\partial k}\right) \tag{B5}$$

Upon integrating by parts,

$$\int_0^\infty k^m \frac{\partial G(k)}{\partial k}\,\mathrm{d}k = (k')^m G(k')\Big|_{k'\to\infty} - m\int_0^\infty k^{m-1}G(k)\mathrm{d}k \tag{B6}$$

For this model, a good approximation for the high wave number spectral behavior of the three quantities a_y, b and R_{nn} is that all three behave as k^m, where m is at most $-5/3$. $G(k)$ remains constant for large values only when one samples the spectrum far enough to the right (away from the influence of a_y). Upon examination of $G(k)$, it can then be seen that $G(k)$ approaches a constant value as $k\to\infty$; thus for all values of m such that $m\le 0$, only the $m=0$ moment will result in a nonzero contribution from the first term on the right side of Eq. (B6). Therefore the moment integral of the cascade terms can be expressed as

$$\int_0^\infty k^m \frac{\partial G(k)}{\partial k}\,\mathrm{d}k = \begin{cases} -m\displaystyle\int_0^\infty k^{m-1}G(k)\mathrm{d}k; \ \text{for } m\neq 0 \\ k^2\sqrt{\dfrac{kR_{nn}}{\bar{\rho}}}\left(-C_1\varphi + C_2 k\dfrac{\partial\varphi}{\partial k}\right)\Big|_{k\to\infty}; \ \text{for } m=0 \end{cases} \tag{B7}$$

The term resulting from the moments for $m\neq 0$ on the right side of Eq. (B7) is a constant that represents the decay of the quantity φ due the cascade action of the turbulence to higher and higher wave numbers.

With the discussion of the cascade terms completed, the self-similar forms from Eq. (B1) are now substituted into the spectral model equations of Article I and the moments for $m = 0$ and the $m = -1$ are calculated. The resulting three transport equations for $a_y(y,t)$, $b(y,t)$ and $K(y,t)$ are (omitting their arguments for brevity)

$$\frac{\partial \bar{\rho} a_y}{\partial t} + \frac{\partial \bar{\rho} a_y \tilde{u}_y}{\partial y} = b\frac{\partial \bar{p}}{\partial y} - \left[N_4 \sqrt{a_n a_n} + I_2 \sqrt{2K\left(\frac{L_R}{L_a}\right)} \right] \frac{\bar{\rho} a_y}{L_a} - N_3 K \frac{\partial \bar{\rho}}{\partial y} + C_D \frac{\partial}{\partial y} \bar{\rho} \upsilon_t \frac{\partial a_y}{\partial y} \tag{B8}$$

$$\frac{\partial b}{\partial t} = \left(\frac{2\bar{\rho} - \rho_1 - \rho_2}{\rho_1 \rho_2} \right) \frac{\partial \bar{\rho} a_y}{\partial y} + I_1 \frac{b}{L_b} \sqrt{2K\left(\frac{L_R}{L_b}\right)} + C_D \frac{\partial}{\partial y} \upsilon_t \frac{\partial b}{\partial y} \tag{B9}$$

$$\frac{\partial \bar{\rho} K}{\partial t} + \frac{\partial \bar{\rho} K \tilde{u}_y}{\partial y} = \int_{+\infty}^{+\infty} a_y(y') \frac{\partial \bar{\rho}(y')}{\partial y} S_0(y, y') \mathrm{d}y' - N_3 \bar{\rho} K \frac{\partial \tilde{u}_y}{\partial y} + C_D \frac{\partial}{\partial y} \upsilon_t \frac{\partial \bar{\rho} K}{\partial y} - N_2 \bar{\rho} \varepsilon \tag{B10}$$

and the three corresponding transport equations of the respective length scales, $L_a(y,t)$, $L_b(y,t)$ and $L_R(y,t)$ are

$$\begin{aligned} \frac{\partial \bar{\rho} L_a}{\partial t} + \frac{\partial \bar{\rho} L_a \tilde{u}_y}{\partial y} = & \left[\left(\frac{N_7}{N_8}\right)\left(\frac{L_b}{L_a}\right) - 1 \right] \frac{b L_a}{a_y} \frac{\partial \bar{\rho}}{\partial y} - N_5 \bar{\rho} \sqrt{a_n a_n} - I_4 \bar{\rho} \sqrt{2K\left(\frac{L_R}{L_a}\right)} \\ & + \left[N_3 - N_6 \left(\frac{L_R}{L_a}\right) \right] \frac{K L_a}{a_y} \frac{\partial \bar{\rho}}{\partial y} + C_D \frac{\partial}{\partial y} \bar{\rho} \upsilon_t \frac{\partial L_a}{\partial y} + \frac{2 C_D \bar{\rho} \upsilon_t}{a_y} \left(\frac{\partial a_y}{\partial y}\right)\left(\frac{\partial L_a}{\partial y}\right) \end{aligned} \tag{B11}$$

$$\begin{aligned} \frac{\partial L_b}{\partial t} = & \left(\frac{2\bar{\rho} - \rho_1 - \rho_2}{b \rho_1 \rho_2} \right) \left[\frac{N_8}{N_7} \frac{\partial \bar{\rho} a_y L_a}{\partial y} - L_b \frac{\partial \bar{\rho} a_y}{\partial y} \right] + C_D \frac{\partial}{\partial y} \upsilon_t \frac{\partial L_b}{\partial y} \\ & - \frac{N_8}{N_7} C_{fb} \left(\frac{\bar{\nu}^2 a_y L_a}{b} \right) \frac{\partial}{\partial y} \left(\frac{\bar{\rho}}{\bar{\nu}} \right) + I_3 \sqrt{2K\left(\frac{L_R}{L_b}\right)} + \frac{2 C_D \upsilon_t}{b} \left(\frac{\partial L_b}{\partial y}\right)\left(\frac{\partial b}{\partial y}\right) \end{aligned} \tag{B12}$$

and

$$\begin{aligned} \frac{\partial \bar{\rho} L_R}{\partial t} + \frac{\partial \bar{\rho} L_R \tilde{u}_y}{\partial y} = & \frac{1}{K} \int_{+\infty}^{+\infty} a_y(y') \frac{\partial \bar{p}(y')}{\partial y} S(y, y') \mathrm{d}y' - N_9 \bar{\rho} L_R \frac{\partial \tilde{u}_y}{\partial y} + N_{10} \bar{\rho} \sqrt{K} \\ & + \bar{\rho} C_D \frac{\partial}{\partial y} \left(\upsilon_t \frac{\partial L_R}{\partial y} \right) + \frac{2 C_D \upsilon_t}{K} \left(\frac{\partial \bar{\rho} K}{\partial y}\right)\left(\frac{\partial L_R}{\partial y}\right) \end{aligned} \tag{B13}$$

where

$$N_1 = \int_0^{\infty} \left(\frac{1}{\xi}\right) F_{nn}(\xi) \mathrm{d}\xi$$

$$N_2 = \left[\xi^2\sqrt{2\xi F_{nn}(\xi)}\left(C_1 F_{nn}(\xi) - C_2\xi F'_{nn}(\xi)\right)\right]_{\xi\to\infty}$$

$$N_3 = 2\int_0^\infty F_{yy}(\xi)\mathrm{d}\xi$$

$$N_4 = C_{\mathrm{rp1}}\int_0^\infty \xi^2 F_a^2(\xi)\mathrm{d}\xi$$

$$N_5 = \left(\frac{C_{\mathrm{rp1}}}{N_8}\right)\int_0^\infty \xi F_a^2(\xi)\mathrm{d}\xi - N_4$$

$$N_6 = \left(\frac{2}{N_8}\right)\int_0^\infty \left(\frac{1}{\xi}\right)F_{yy}(\xi)\mathrm{d}\xi$$

$$N_7 = \int_0^\infty \left(\frac{1}{\xi}\right)F_b(\xi)\mathrm{d}\xi$$

$$N_8 = \int_0^\infty \left(\frac{1}{\xi}\right)F_a(\xi)\mathrm{d}\xi$$

$$N_9 = \left(\frac{2}{N_1}\right)\int_0^\infty \left(\frac{1}{\xi}\right)F_{yy}(\xi)\mathrm{d}\xi - N_3$$

$$N_{10} = -N_2 + \left(\frac{1}{N_1}\right)\int_0^\infty \left[\sqrt{2\xi F_{nn}(\xi)}\left(-C_1 F_{nn}(\xi) + C_2\xi F'_{nn}(\xi)\right)\right]\mathrm{d}\xi$$

$$+\left(\frac{1}{N_1}\right)\xi\sqrt{2F_{nn}(\xi)}\left[-C_1 F_{nn}(\xi) + C_2\xi F'_{nn}(\xi)\right]_{\xi\to\infty}$$

$$I_1 = \left[\xi^2\sqrt{\xi F_{nn}\left[\xi\left(\frac{L_R}{L_b}\right)\right]}\left(-C_1 F_b(\xi) + C_2\xi F'_b(\xi)\right)\right]_{\xi\to\infty}$$

$$I_2 = C_{\mathrm{rp2}} \int_0^\infty \xi F_a(\xi) \sqrt{\xi F_{nn}\left[\xi\left(\frac{L_R}{L_a}\right)\right]}\,\mathrm{d}\xi$$

$$I_3 = \left(\frac{1}{N_7}\right) \int_0^\infty \left[\sqrt{\xi F_{nn}\left[\xi\left(\frac{L_R}{L_a}\right)\right]}\left(-C_1 F_b(\xi) + C_2 \xi F'_b(\xi)\right)\right] \mathrm{d}\xi - I_1$$

$$I_4 = \left(\frac{C_{\mathrm{rp2}}}{N_8}\right) \int_0^\infty F_a(\xi) \sqrt{\xi F_{nn}\left[\xi\left(\frac{L_R}{L_a}\right)\right]}\,\mathrm{d}\xi - I_2$$

$$- \left(\frac{1}{N_8}\right) \int_0^\infty \sqrt{\xi F_{nn}\left[\xi\left(\frac{L_R}{L_a}\right)\right]}\left(-C_1 F_a(\xi) + C_2 \xi F'_a(\xi)\right) \mathrm{d}\xi$$

$$- \left(\frac{1}{N_8}\right) \int_0^\infty \left[\sqrt{\xi F_{nn}\left[\xi\left(\frac{L_R}{L_a}\right)\right]}\left(-C_1 F_a(\xi) + C_2 \xi F'_a(\xi)\right)\right] \mathrm{d}\xi$$

$$S_0(y, y') = \int_0^\infty F_a(\xi) S_1(y, y', \xi)\,\mathrm{d}\xi$$

$$S(y, y') = \left(\frac{L_a(y')}{N_1}\right) \int_0^\infty \left(\frac{1}{\xi}\right) F_a(\xi) S_1(y, y', \xi)\,\mathrm{d}\xi - L_R(y) S_0(y, y')$$

$$S_1(y, y', \xi) = \frac{\exp\left[-2\xi\left|\dfrac{y' - y}{L_a(y')}\right|\right]}{\displaystyle\int_{+\infty}^{+\infty} \exp\left[-2\xi\left|\frac{y'' - y}{L_a(y')}\right|\right] \mathrm{d}y''}$$

and

$$\varepsilon = \frac{K\sqrt{K}}{L_R}$$

Note that the decay term due to molecular diffusion in the $b(y,t)$ equation has been omitted since we have neglected this effect in this study. Note the persistence of the nonlocality in both the transport equation for $K(y,t)$ and its length scale $L_R(y,t)$. This nonlocal contribution represents an extension of the physics that is currently implemented in the formulation of

single-point model equations. Another enhancement to single point models, as derived by Steinkamp (1996), is the density–mass–flux gradient source term to $b(y,t)$.

References

Allred, J.C., Blount, G.H., 1953. Experimental studies of Taylor instability. Los Alamos National Laboratory Report, LA-1600. Los Alamos, NM, USA.

Andrews, M.J., 1986. Turbulent mixing by Rayleigh–Taylor instability. CFDU report no. CFDU/86/10. (Ph.D. Dissertation).

Andrews, M.J., 1992. An experimental study of turbulent mixing by Rayleigh–Taylor instabilities and a two-fluid model of the mixing phenomena. In: W.P. Dannevik, A.C. Buckingham, C.E. Leith (Ed.). Advances in Compressible Turbulent Mixing. National Technical Information Service, US Department of Commerce, pp. 7–19.

Andrews, M.J., Spalding, D.B., 1990. A simple experiment to investigate two-dimensional mixing by Rayleigh–Taylor instability. Phys. Fluids A 2(6), 922–927.

Andronov, V.A., Bakhrakh, S.M., Meshkov, E.E., Mokhov, V.V., Nikiforov, V.V., Pevnitshii, A.V., Tolshmyakov, A.I., 1976. Turbulent mixing at contact surface accelerated by shock waves. Sov. Phys. JETP 44, 424–427.

Anisimov, V.I., Polyonov, A.V., 1989. The statistical model of the turbulent mixing zone and its applying to the experiments analysis. In: In: Proceedings of 1st International Workshop on Compressible Turbulent Mixing. Pleasanton, CA, USA.

Anuchina, N.N., Kucherenko, YuA, Neuvazhaev, V.E., Ogibina, V.N., Shibarshov, L.I., Yakovlev, V.G., 1978. Turbulent mixing at the accelerating interface between fluids. Mech. Fluids 6, 157.

Belenkii, S.Z., Fradkin, E.S., 1965. The theory of turbulent mixing. Papers Phys. Ins. AS USSR 29, .

Bellman, R., Pennington, R.H., 1954. Effects of surface tension and viscosity on Taylor instability. Q. App. Math. 12, 151–162.

Besnard DC, Harlow FH, Rauenzahn RM, 1987, Conservation and transport properties of turbulence with large density variations, Los Alamos National Laboratory Report LA-10911-MS, Los Alamos, NM, USA, (Also see: Besnard DC, Harlow FH, Rauenzahn RM, Zemach C, 1992, Turbulence transport equations for variable density turbulence and their relationships to two-field models, Los Alamos National Laboratory Report LA-12303-MS. Los Alamos, NM, USA).

Besnard, D.C., Harlow, F.H., Rauenzahn, R.M., Zemach, C., 1992. Turbulence transport equations for variable density turbulence and their relationships to two-field models. Los Alamos National Laboratory Report LA-12303-MS. Los Alamos, NM, USA.

Besnard, D., Ducros, F., Loreaux, Ph, Mimouni, S., Vasseur, A., 1995. Turbulent mixing modeling and simulation. In: J. Glimm, J. Groves, R. Young (Ed.). In: Proceedings of 5th International Workshop on the Physics of Compressible Turbulent Mixing. State University of New York, Stony Brook, NY, USA, Preprint.

Besnard DC, Harlow FH, Rauenzahn RM, Zemach C, 1996, Spectral transport model for turbulence, Theor. Comp. Fluid Dyn., 8, 1–35, (Also see: Besnard DC, Harlow FH, Rauenzahn RM, Zemach C, 1990, Spectral transport model for turbulence, Los Alamos National Laboratory Report LA-11821-MS, Los Alamos, NM, USA).

Birkhoff, G., 1954. Taylor instability and laminar mixing. Los Alamos Scientific Laboratory Report LA-1862. Los Alamos, NM, USA.

Birkhoff, G., 1956. Taylor instability appendices to report LA-1862. Los Alamos Scientific Laboratory Report, LA-1927. Los Alamos, NM, USA.

Burrows, K.D., Smeeton, V.S., Youngs, D.L., 1984. Experimental investigation of turbulent mixing by Rayleigh–Taylor instability, II. United Kingdom Atomic Weapons Research Establishment Report 0 22/84. Aldermaston, UK.

Case, K.M., 1960. Taylor instability of an inverted atmosphere. Phys. Fluids 3, 366–368.

Chandrasekhar, S., 1954. Stochastic problems in physics and astronomy. In: N. Wax (Ed.). Selected Papers on Noise and Stochastic Processes. Dover, New York, pp. 1–89.

Clark, T.T., Spitz, P.B., 1995. Two-point correlation equations for variable density turbulence. Los Alamos National Laboratory Report, LA-12671-MS. Los Alamos, NM, USA.

Clark TT, Zemach C, 1995, A spectral model applied to homogeneous turbulence, Phys. Fluids, 7, 1674–1694, (Also see: Clark TT, 1992, Spectral self-similarity of homogeneous anisotropic turbulence, Los Alamos National Laboratory Report, LA-12284-T. Los Alamos, NM, USA).

Cole, R.L., Tankin, R.S., 1973. Experimental study of Taylor instability. Phys. Fluids 16, 1810–1815.
Cranfill, C.W., 1991. A multifluid turbulent-mix model. Los Alamos National Laboratory Report, LA-UR-91-403. Los Alamos, NM, USA.
Daly, B.J., 1967. Numerical study of two fluid Rayleigh–Taylor instability. Phys. Fluids 10, 297–307.
Daly, B.J., 1969. Numerical study of the effect of surface tension on interface instability. Phys. Fluids. 12, 1340–1354.
Davies, R.M., Taylor, G.I., 1949. The mechanics of large bubbles rising through extended liquids and through liquids in tubes. Proc. Roy. Soc. Lond. A 200, 375–390.
Drew, D.A., 1983. Mathematical modeling of two-phase flow. Ann. Rev. Fluid Mech. 15, 261–291.
Duff, R.E., Harlow, F.H., Hirt, C.W., 1962. Effects of diffusion on interface instability between gases. Phys. Fluids 5, 417–425.
Emmons, H.W., Chang, C.T., Watson, B.C., 1960. Taylor instability of finite surface waves. J. Fluid Mech. 7, 177–193.
Gardner, C.L., Glimm, J., McBryan, O., Menikoff, R., Sharp, D.H., Zhang, Q., 1988. The dynamics of bubble growth for Rayleigh–Taylor unstable interface. Phys. Fluids A 31, 447–465.
Glimm, J., Li, X.L., Zhang, Q., Menikoff, R., Sharp, D., 1992. Statistical theories of Rayleigh–Taylor instability for compressible fluids. In: W.P. Dannevik, A.C. Buckingham, C.E. Leith (Ed.). Advances in Compressible Turbulent Mixing. National Technical Information Service, US Department of Commerce, pp. 85–93.
Harlow, F.H., Welch, J.E., 1965. Numerical calculation of time-dependent viscous incompressible flow of fluid with free surface. Phys. Fluids 8, 2182–2189.
Hide, R., 1955. The character of the equilibrium of an incompressible heavy viscous fluid of variable density: An approximate theory. Proc. Cambridge Phil. Soc. 51, 179–201.
Jeandel, D., Brison, J.F., Mathieu, J., 1978. Modeling methods in physical and spectral space. Phys. Fluids 21 (2), 169–182.
Kucherenko, YuA, Shibarshov, L.I., 1986. Turbulent mixing at the plane interface between media with different densities and being subjected to the series of delta-shaped accelerations. Prob. Atomic Sci. Engng. (Ser. Theor. Appl. Phys.) 2, 3.
Kucherenko, YuA, Shibarshov, L.I., Chitaikin, V.I., Balabin, S.I., Pylaev, A.P., 1991. Experimental study of the gravitational turbulent mixing self-similar mode. Proceedings of 3rd International Workshop on the Physics of Compressible Turbulent Mixing. Abbey of Royaumont, France, pp. 427–454.
Kucherenko, YuA, Neuvazhaev, V.E., Pylaev, A.P., 1994. Behavior of a region of gravity-induced turbulent mixing under conditions leading to separation. Physics-Doklady (Official English Translation of Doklady Akademii Nauk) 39, 114–117.
Lamb, H., 1931. Hydrodynamics, 6th ed. Edition. Dover, New York, p. 370, 378, 456, 625.
LeLevier, R., Lasher, G.J., Bjorklund, F., 1955. Effect of a density gradient on Taylor instability. University of California Radiation Laboratory Report UCRL-4459. Livermore, CA, USA.
Lesieur, M., Schertzer, D., 1978. Amortissement autosimilaire d'une turbulence à grand nombre de Reynolds. J. Méc. 17 (14), 609–645.
Lewis, D.J., 1950. The instability of liquid surfaces when accelerated in a direction perpendicular to their planes. II. Proc. Roy. Soc. Lond. A202, 81–96.
Li, X.L., 1993. Study of three-dimensional Rayleigh–Taylor instabilities in compressible fluids through level set method and parallel computation. Phys. Fluids A 5, 1904–1913.
Linden, P.F., Redondo, J.M., Caulfield, C.P., 1992. Molecular mixing in Rayleigh–Taylor instability. In: W.P. Dannevik, A.C. Buckingham, C.E. Leith (Ed.). Advances in Compressible Turbulent Mixing. National Technical Information Service, US Department of Commerce, pp. 95–104.
Linden, P.F., Redondo, J.M., Youngs, D.L., 1994. Molecular mixing in Rayleigh–Taylor instability. J. Fluid Mech. 265, 97–124.
Meshkov, E.E., 1969. Instability of the interface of two gases accelerated by a shock wave. Fluid Dyn. 4, 101 [Izv. Akad. Nauk SSSR, Mekh. Zhidk. Gaza 5, 151 (1969)].
Mitchner, M., Landshoff, R.K.M., 1964. Rayleigh–Taylor instability for compressible fluids. Phys. Fluids. 7, 862–866.
Neuvazhaev, V.E., 1989. Numerical calculation of interfaces turbulent mixing by Rayleigh–Taylor instability on the basis of semi-empirical models. Proceedings of 1st International Workshop on Compressible Turbulent Mixing. Pleasanton, CA, USA.

Neuvazhaev, V.E., Yakovlev, V.G., 1984. Model and method for numerical calculation of turbulent mixing interfaces moving with acceleration. Prob. Atomic Sci. Engng. (Ser. Meth. Prog. Numer. Solution Math. Phys. Prob.) 2, 17.

Nikiforov, V.V., 1991. Calculation of gravitational turbulent mixing in non-automodel flows. Proceedings of 2nd International Workshop on the Physics of Compressible Turbulent Mixing. Cambridge, UK, pp. 478–496.

Nikiforov, V.V., 1994. Personal communication. All Russian Research Institute of Experimental Physics, Arzamas-16, Russia.

Polyonov, A.V., 1989. The heterogeneous K–ε model of gravitational mixing. Proceedings of 1st International Workshop on Compressible Turbulent Mixing. Pleasanton, CA, USA.

Popil, R., Curzon, F.L., 1979. Production of reproducible Rayleigh–Taylor instabilities. Rev. Sci. Instrum. 50, 1291–1295.

Ratafia, M., 1973. Experimental investigation of Rayleigh–Taylor instability. Phys. Fluids 16, 1207–1210.

Lord, Rayleigh, 1900. Investigation of the character of the equilibrium of an incompressible heavy fluid of variable density. Scientific Papers 2, 200–207 (Cambridge, UK).

Read, K.I., 1984. Experimental investigation of turbulent mixing by Rayleigh–Taylor instability. Physica 12D, 45–58.

Read, K.I., Youngs, D.L., 1983. Experimental investigation of turbulent mixing by Rayleigh–Taylor instability. United Kingdom Atomic Weapons Research Establishment report 011/83, Aldermaston, UK.

Remington, B.A., Dimonte, G., 1995. Personal communications. Lawrence Livermore National Laboratory, Livermore, CA, USA.

Richtmyer, R.D., 1960. Taylor instability in shock acceleration of compressible fluids. Commun. Pure Appl. Math. 13, 297–319.

Sharp, D.H., 1984. An overview of Rayleigh–Taylor instability. Physica D12, 3–18.

Smeeton, V.S., Youngs, D.L., 1987. Experimental investigation of turbulent mixing by Rayleigh–Taylor instability, Part 3. United Kingdom Atomic Weapons Research Establishment report O 35/87, Aldermaston, UK.

Snider, D.M., Andrews, M.J., 1994. Rayleigh–Taylor and shear driven mixing with an unstable thermal stratification. Phys. Fluids 6, 3324–3334.

Spalding, D.B., 1985a. Two-fluid models of turbulence. CFD report no. CFDU/85/4, Imperial College, London.

Spalding, D.B., 1985b. The numerical computation of multi-phase flows. CFD report no. CFDU/85/7, Imperial College, London.

Steinkamp, M.J., 1996. A spectral model for variable density turbulent mixing. Los Alamos National Laboratory Report LA-13123-T, Los Alamos, NM, USA.

Takabe, H., Mima, K., Montierth, L., Morse, R.L., 1985. Self-consistent growth rate of the Rayleigh–Taylor instability in an ablatively accelerating plasma. Phys. Fluids 28, 3676–3682.

Taylor, G.I., 1950. The instability of liquid surfaces when accelerated in a direction perpendicular to their plane. I. Proc. R. Soc. Lond. A201, 192–196.

Tryggvason, G., 1988. Numerical simulations of the Rayleigh–Taylor instability. J. Comput. Phys. 75, 253–282.

Tryggvason, G., Unverdi, S.O., 1990. Computations of three-dimensional Rayleigh–Taylor instability. Phys. Fluids A 2 (5), 656–659.

Welch, J.E., Harlow, F.H., Shannon, J.P., Daly, B.J., 1966. The MAC method. Los Alamos Scientific Laboratory report LA-3425, Los Alamos, NM, USA.

Youngs, D.L., 1984. Numerical simulation of turbulent mixing by Rayleigh–Taylor instability. Physica D12, 32–44.

Youngs, D.L., 1989. Modelling turbulent mixing by Rayleigh–Taylor instability. Physica D37, 270–287.

Youngs, D.L., 1991. Three-dimensional numerical simulation of turbulent mixing by Rayleigh–Taylor instability. Phys. Fluids A3 (5), 1312–1320.

Youngs, D.L., 1992a. Experimental investigation of turbulent mixing by Rayleigh–Taylor instability. In: W.P. Dannevik, A.C. Buckingham, C.E. Leith (Ed.). Advances in Compressible Turbulent Mixing. National Technical Information Service, US Department of Commerce, pp. 607–626.

Youngs, D.L., 1992b. A two-dimensional turbulence model based on the equations of multiphase flow. Proceedings of the Third Zababakhin Scientific Talks. Kyshtym, USSR.

Youngs, D.L., 1993. Personal communications. United Kingdom Atomic Weapons Research Establishment, Aldermaston, UK.

Youngs, D.L., 1994. Numerical simulation of mixing by Rayleigh–Taylor and Richtmyer–Meshkov instabilities. Laser Particle Beams 12, 725–750.